Three-dimensional diffusion simulation of outer radiation belt electrons during the 9 October 1990 magnetic storm

Jay M. Albert,[1] Nigel P. Meredith,[2] and Richard B. Horne[2]

[1] Relativistic (>1 MeV) electron flux increases in the Earth's radiation belts are significantly underestimated by models that only include transport and loss processes, suggesting that some additional acceleration process is required. Here we use a new, three-dimensional code that includes radial diffusion and quasi-linear pitch angle and energy diffusion due to chorus waves, including cross terms, to simulate the 9 October 1990 magnetic storm. The diffusion coefficients are activity dependent, and time-dependent boundary conditions are imposed on all six boundary faces, taken from fits to CRRES Medium Electrons A electron data. Although the main phase dropout is not fully captured, the persistent phase space density peaks observed during the recovery phase are well explained, but this requires both chorus wave acceleration and radial diffusion.

1. Introduction

[2] Outer zone radiation belt electrons exhibit highly dynamic behavior during geomagnetic storms. It has been well documented that the energetic flux drops rapidly during the storm main phase but recovers over several days, often to higher than original levels. Radial diffusion accelerates particles (as they move inward at constant first and second adiabatic invariant) but is hard pressed to reproduce the rate and extent of the recovery, especially when losses are considered, without an additional source of energization.

[3] The moderate storm that occurred on 9 October 1990 has been particularly well studied because of its detailed observation by CRRES. *Brautigam and Albert* [2000] simulated it with activity-dependent radial diffusion and a realistic, variable outer boundary condition. Plasmaspheric hiss was the only loss process considered. This model was found to work reasonably well for electrons with first adiabatic invariant $M \approx 100-300$ MeV/G but was unable to account for the increase, and inward pointing phase space density gradient, for $M \approx 700-1000$ MeV/G. Many other one-dimensional simulations of radial diffusion have been performed, usually with time scale estimates for wave-induced losses [e.g., *Shprits and Thorne*, 2004; *Shprits et al.*, 2005, 2006b; *Fei et al.*, 2006; *Lam et al.*, 2007] and with an estimated internal source term [*Tu et al.*, 2009]. The results are mixed but generally support the finding that radial diffusion is insufficient.

[4] Energy diffusion, caused by cyclotron resonant interactions with whistler mode chorus waves, is frequently invoked as a candidate mechanism for additional energization [*Horne and Thorne*, 1998; *Summers et al.*, 1998]. Indeed, the gradual acceleration of electrons to relativistic energies during the recovery phase of the 9 October 1990 storm was associated with prolonged substorm activity as monitored by the AE index, electron injections at subrelativistic energies, and enhanced chorus amplitudes [*Meredith et al.*, 2002]. Furthermore, flat topped electron pitch angle distributions, characteristic of pitch angle and energy scattering by resonant wave-particle interactions with whistler mode chorus waves, developed at MeV energies [*Horne et al.*, 2003]. Much work has been done in recent years to document enhanced chorus waves during storms [e.g., *Meredith et al.*, 2003a; *Smith et al.*, 2004], to evaluate the corresponding quasi-linear diffusion coefficients [*Albert*, 2005; *Glauert and Horne*, 2005], and to estimate the particle evolution using a one-dimensional (1-D) energy diffusion equation [e.g., *Summers and Ma*, 2000; *Summers et al.*, 2002; *Horne et al.*, 2005a, 2005b].

[5] Several idealized 2-D simulations of diffusion in pitch angle and energy near $L = 4.5$ have been done, accounting for chorus waves [*Albert and Young*, 2005; *Shprits et al.*, 2006a; *Tao et al.*, 2008; *Xiao et al.*, 2009], hiss combined with magnetosonic waves [*Tao et al.*, 2009], and chorus waves combined with VLF hiss and electromagnetic ion cyclotron (EMIC) waves in high-density plumes [*Li et al.*, 2007]. None of these studies included radial diffusion. No studies seem to have solved the local diffusion equation with radial diffusion treated as a source or loss term, although *Thorne et al.* [2007] used lifetimes, obtained from a pitch angle diffusion equation, in separate 1-D equations for radial diffusion and energy diffusion.

[6] Some preliminary three-dimensional simulations, including radial, pitch angle, and energy diffusion, have been performed [*Varotsou et al.*, 2005, 2008; *Subbotin et al.*, 2008]. Furthermore, some progress has been made in adding pitch angle and energy diffusion to advection-driven ring

---

[1]Space Vehicles Directorate, Air Force Research Laboratory, Hanscom Air Force Base, Massachusetts, USA.
[2]British Antarctic Survey, Natural Environment Research Council, Cambridge, UK.
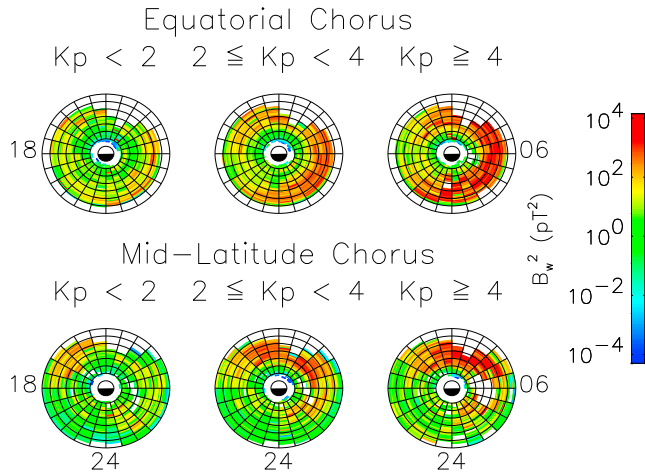
Figure 1. Models of the chorus wave magnetic field intensity, based on CRRES measurements, used to calculate pitch angle and energy diffusion coefficients for different ranges of Kp.

current codes, which are bounce averaged but not drift averaged and so are essentially four dimensional. *Fok et al.* [2008] treated pitch angle and energy diffusion by chorus, while *Jordanova et al.* [2008] included pitch angle diffusion by EMIC waves.

[7] It is widely believed that the generation of chorus waves inherently involves nonlinear wave-particle coupling [e.g., *Nunn*, 1974; *Nunn et al.*, 1997; *Katoh and Omura*, 2007a, 2007b]. However, the particles involved are generally of much lower energy than the ones considered here, which are taken to interact "parasitically" with fully developed chorus. Individual, coherent whistler mode waves can lead to particle diffusion, phase trapping, or phase bunching (without trapping), depending primarily on the competing effects of wave amplitude and background magnetic field inhomogeneity at resonance [*Albert*, 2000, 2002; *Trakhtengerts et al.*, 2003; *Omura and Summers*, 2006; *Demekhov et al.*, 2006; *Bortnik et al.*, 2008]. However, the applicability of this picture to the global evolution of energetic particle distributions during storm conditions has not yet been established. This paper is based on quasi-linear diffusion both because to some extent "it seems to work" and as a basis for comparison with future developments in nonlinear modeling.

[8] This paper combines diffusion by chorus waves with radial diffusion in a carefully chosen three-dimensional grid. Cross diffusion, which was not treated by any of the papers just cited except *Albert and Young* [2005], *Tao et al.* [2008, 2009], and *Xiao et al.* [2009], is included. CRRES Medium Electrons A (MEA) data are used to evaluate time-dependent boundary conditions at low and high E and α_0, as well as at high and low L. This required substantial fitting, interpolation, and extrapolation of the data, as described in section 3. The particle data were used to drive the boundaries only; after initialization, data were not assimilated into the interior of the grid (as was done by *Shprits et al.* [2007]).

2. Diffusion Equation

[9] Cyclotron resonant wave-particle interactions break the first two adiabatic invariants, while drift resonant electric and magnetic fluctuations break only the third invariant. The assumptions of continuous, small, uncorrelated resonances lead to a multidimensional diffusion equation for the phase space density, f, written as

$$\frac{\partial f}{\partial t} = \frac{\partial}{\partial J_1}\left(D_{11}\frac{\partial f}{\partial J_1} + D_{12}\frac{\partial f}{\partial J_2}\right) + \frac{\partial}{\partial J_2}\left(D_{12}\frac{\partial f}{\partial J_1} + D_{22}\frac{\partial f}{\partial J_2}\right) + \frac{\partial}{\partial J_3}D_{33}\frac{\partial f}{\partial J_3}. \tag{1}$$

The cyclotron frequency and drift frequency interactions are considered uncoupled, so no terms involving D_{13} or D_{23} are included.

[10] It is common to change variables from (J_1, J_2, J_3) to (α_0, E, L), where L (often denoted L^*) labels the drift shell [*Roederer*, 1970], E is energy, and α_0 denotes equatorial pitch angle. Actually, in a nonaxisymmetric magnetic field, the minimum (equatorial) value of α will vary for different magnetic field lines of a particle's drift shell. However, it is reasonable to relate the two sets of variables using the expressions suitable for a dipole field. This can be considered simply a convenient change of variables, as long as the invariants are properly computed in a realistic magnetic field model, and gives

$$\frac{\partial f}{\partial t} = \frac{1}{G}\frac{\partial}{\partial \alpha_0}G\left(\frac{D_{\alpha_0\alpha_0}}{p^2}\frac{\partial f}{\partial \alpha_0} + \frac{D_{\alpha_0 p}}{p}\frac{\partial f}{\partial p}\right) + \frac{1}{G}\frac{\partial}{\partial p}G\left(\frac{D_{\alpha_0 p}}{p}\frac{\partial f}{\partial \alpha_0} + D_{pp}\frac{\partial f}{\partial p}\right) + L^2\frac{\partial}{\partial L}\frac{D_{LL}}{L^2}\frac{\partial f}{\partial L}, \tag{2}$$

where $G = p^2 T(\alpha_0)\sin\alpha_0\cos\alpha_0$ [*Schulz*, 1991] and $T(\alpha_0) \approx 1.30 - 0.56\sin\alpha_0$ is the normalized bounce period [e.g., *Lyons et al.*, 1972]. It is understood that the L derivatives are evaluated at fixed (J_1, J_2), not fixed (α_0, p). Because E and p are simply related, terms like "energy diffusion" and "diffusion in p" will often be used interchangeably.

2.1. Pitch Angle and Energy Diffusion Coefficients

[11] The pitch angle and energy diffusion coefficients are evaluated according to bounce- and drift-averaged quasi-linear theory [*Albert*, 2005; *Glauert and Horne*, 2005], requiring models of wave intensity, B_w^2, and its distribution in frequency and wave normal angle, as well as values of the plasma frequency-to-gyrofrequency ratio, f_{pe}/f_{ce}. As mentioned, only whistler mode chorus waves will be considered. Values of B_w^2 and f_{pe}/f_{ce} were taken from statistical maps of CRRES observations, compiled with resolution of 1 h in magnetic local time and 0.1 in L. The maps were also parameterized by Kp (into three ranges: $Kp < 2$, $2 \leq Kp < 4$, and $Kp \geq 4$), and by latitude ("equatorial," within 15° of the equator, and "midlatitude," 15°−30° off the equator). The resulting values are shown in Figures 1 and 2. A similar model, parameterized by AE, was presented by *Meredith et al.* [2003b].

[12] The frequency and wave normal angle distributions were represented, as usual, by truncated Gaussians. The peak, width, lower cutoff, and upper cutoff for ω and $x = \tan\theta$ were $(\omega_m, \delta\omega, \omega_{LC}, \omega_{UC}) = (0.35, 0.15, 0.125, 0.575)\Omega_{eq}$ and $(x_m, \delta x, x_{min}, x_{max}) = (0, \tan 30°, 0, 1)$, respectively.
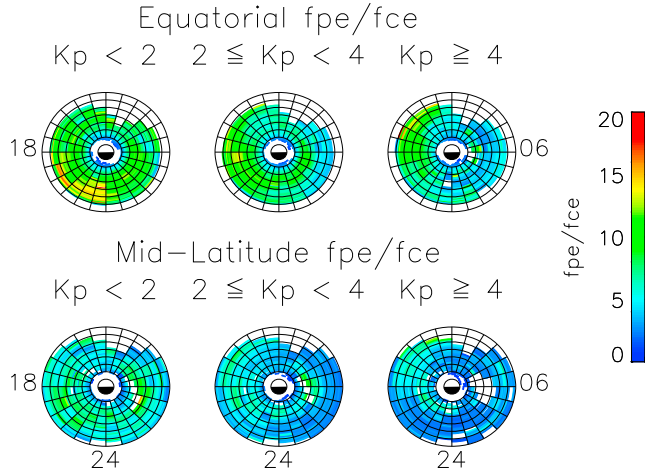
Figure 2. Models of equatorial f_{pe}/f_{ce}, based on CRRES measurements, used to calculate pitch angle and energy diffusion coefficients for different ranges of Kp.

These were used to compute tables of diffusion coefficients for 89 integer values of α_0, 40 values of E between 0.01 and 10 MeV, and 9 values of f_{pe}/f_{ce} between 1 and 20, using the computational techniques of *Albert* [2005]. These tables were then scaled in B_w^2 and interpolated in f_{pe}/f_{ce}, in conjunction with the statistical maps, to obtain drift-averaged diffusion coefficients for the three ranges of Kp. A very similar procedure was followed by *Varotsou et al.* [2008]. Results at $L = 4.55$ are shown in Figure 3.

2.2. Radial Diffusion Coefficients

[13] Electric and magnetic radial diffusion coefficients, $D_{LL} = D_e + D_m$, were taken from *Brautigam and Albert* [2000] and are also Kp dependent. The magnetic contribu-

tion is given as $D_m = 10^{0.506 Kp - 9.325} L^{10}$ (units are per day), while

$$D_e = \frac{1}{4} \frac{c^2}{R_e^2} \frac{\tilde{E}^2}{B_0^2} \frac{T}{1 + (\omega_D T/2)^2} L^6. \qquad (3)$$

This expression is in Gaussian units, with $B_0 \approx 0.31$ G, and is based on electric field fluctuations with $\tilde{E}$ and the fluctuation decay time T given by

$$\tilde{E} = E_0 + E_1(Kp - 1) \qquad T = 2700 \text{ s}, \qquad (4)$$

with numerical values $E_0 = 3.33 \times 10^{-9}$ statvolt/cm (0.1 mV/m) and $E_1 = 8.67 \times 10^{-9}$ statvolt/cm (0.26 mV/m). The drift frequency ω_D may be written as

$$\omega_D = \frac{3}{2} L \frac{m_e c}{e B_0} \frac{c^2}{R_e^2} \frac{(p/mc)^2 \sin^2 \alpha_0}{\sqrt{1 + (p/mc)^2 \sin^2 \alpha_0}}. \qquad (5)$$

Representative values of D_{LL} are also shown in Figure 3.

2.3. Variables and Grids

[14] Radial diffusion occurs at constant first and second adiabatic invariant, so it is most simply treated in the variables (J_1, J_2, J_3). Cyclotron resonant interactions are more naturally expressed as diffusion in pitch angle and energy, both because the boundaries correspond more closely to real particle detectors and because terms involving cross diffusion are typically dominated by pitch angle diffusion. However, cross diffusion, which expresses the physical relationship between resonant changes in α_0 and p, can have significant consequences, since typically $D_{\alpha_0\alpha_0}/p^2 > |D_{\alpha_0 p}|/p > D_{pp}$. Thus, it is preferable to retain it despite the numerical difficulties it presents to straightforward finite differencing in (α_0, E, L) [*Albert*, 2004,
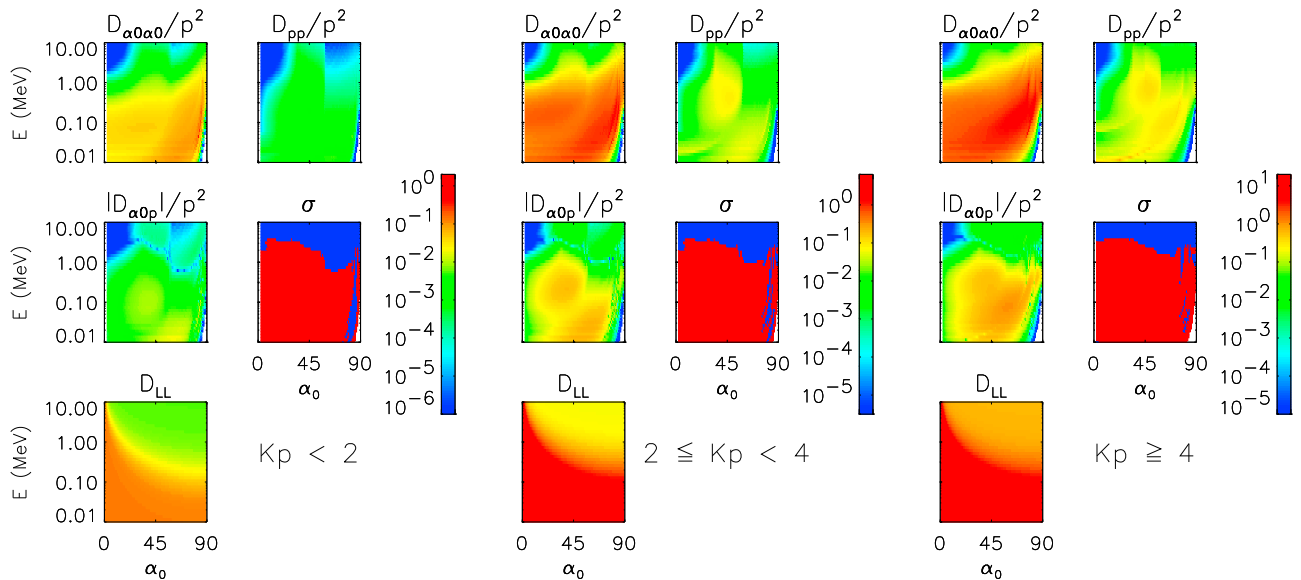

Figure 3. Diffusion coefficients at $L = 4.55$, units are per day. The sign of $D_{\alpha_0 p}$ is indicated by σ (red for positive, blue for negative). D_{LL} is evaluated at $Kp = 1$, $Kp = 3$, and $Kp = 5$.
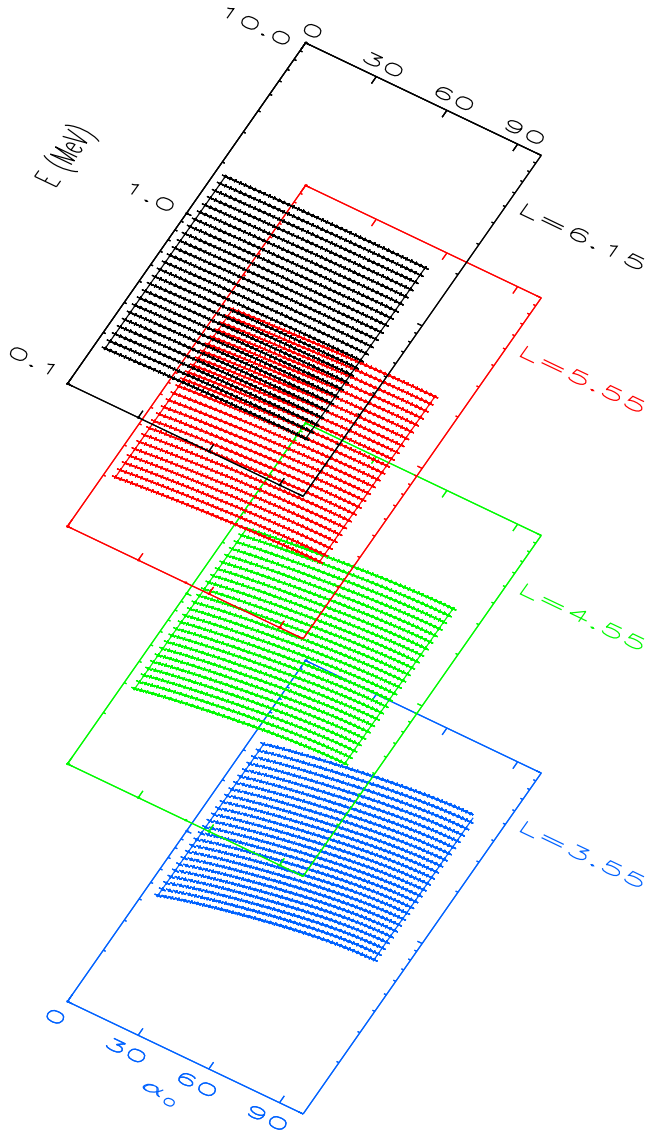
Figure 4. The 3-D computational grid, in (α_0, E, L) space.

[16] Since the points are not regularly aligned in the (Q_1, Q_2) plane, finite differencing requires interpolation in Q_2, though not in Q_1 (since the mapping in L preserves alignment in $Q_1 \equiv \alpha_0$). Exactly analogous interpolation would be required even without cross diffusion, since the mapped points are not aligned in the (α_0, E) plane either [*Subbotin et al.*, 2008]. This procedure was carried out using diffusion coefficients for each of the three Kp ranges. When the appropriate range of Kp changes in the course of a run, the values of (Q_1, Q_2) (and D_1, D_2, Γ) are changed, but the grid points retain their values of α_0, E, L, and f.

[17] Figure 4 illustrates how mapping in L shifts and distorts the range of E. At $L = 6.15$, the computational grid covers $E = 0.2{-}2$ MeV, while at $L = 3.55$ this becomes roughly $0.5{-}4$ MeV. With this scheme, there are no wasted grid points; all of the grid points can couple to the computational domain through diffusion in all of the variables. Figure 5 shows the grid points in more detail in (α_0, E) planes at several values of L. Also shown are the same physical points plotted in (Q_1, Q_2) coordinates (evaluated for $Kp < 2$), as well as in (J_1, J_2) coordinates. Grid points plotted in red lie within the energy range of the CRRES MEA detector so that actual measurements are at least potentially available to initialize the flux values and for comparison during the simulation.

3. CRRES MEA Data Processing

[18] The version of MEA data used by *Brautigam and Albert* [2000] was limited by both saturation and contamination by high-energy protons, which prohibited the use of the two lowest energy channels. The version used here, available through the National Space Science Data Center, has been reprocessed, including a "foldover correction," which overcomes these limitations [*Vampola*, 1998; *Lemaire et al.*, 1998]. Thus, this MEA data set provides flux at $\alpha = 5, 10, \ldots, 90°$, and 17 values of energy ($E = 0.148$ MeV to 1.581 MeV), every 60 s. The problem is to determine values at points (α_i, E_j, L_k) of the computational grid, at any time t. (For grid points, α_i means equatorial pitch angle α_0.)

[19] The CRRES ephemeris files used provide time-tagged satellite location and local magnetic field B every 30 s. For each entry, the Office National d'Etudes et de Recherche Aérospatiales code [*Boscher et al.*, 2008] was used with the Olson-Pfitzer quiet and International Geomagnetic Reference Field magnetic field models to determine and the adiabatic invariants K and L corresponding to the 18 local pitch angle values. (L depends weakly on α but not on energy. K is defined to be proportional to $J_2/\sqrt{J_1}$ [*Schulz*, 1991] so that it is also independent of energy.) Results with L within $\delta L = 0.05$ of a grid value L_k were recorded, along with the earliest and latest times, t_1 and t_2, of each "visit" to each L_k. Equatorial pitch angles α_0 were then determined from

2009]. These difficulties may be overcome in a number of ways [*Albert and Young*, 2005; *Tao et al.*, 2008, 2009; *Xiao et al.*, 2009].

[15] The method of *Albert and Young* [2005] used the diffusion coefficients themselves to constructs new variables, (Q_1, Q_2) at a fixed L, in which cross diffusion vanished; it consisted of choosing $Q_1 = \alpha_0$ and integrating a differential equation for curves of constant Q_2. This can be carried out independently at each L. To make radial diffusion easy to implement, the three-dimensional grid is generated from a convenient set of (α_0, E) at one L value, mapped to other L at constant J_1 and J_2 as in a dipole field, and then converted to (Q_1, Q_2). This gives

$$\frac{\partial f}{\partial t} = \frac{1}{\Gamma}\left(\frac{\partial}{\partial Q_1}\Gamma D_1 \frac{\partial f}{\partial Q_1} + \frac{\partial}{\partial Q_2}\Gamma D_2 \frac{\partial f}{\partial Q_2}\right) + L^2 \frac{\partial}{\partial L}\frac{D_{LL}}{L^2}\frac{\partial f}{\partial L}, \quad (6)$$

where $\Gamma = |\partial(J_1, J_2)/\partial(Q_1, Q_2)|$, and again radial diffusion operates at fixed (J_1, J_2), not fixed (Q_1, Q_2).

$$\frac{Y(\sin\alpha_0)}{\sin\alpha_0} = \frac{K}{L R_e \sqrt{B_{eq}}},$$

where R_e is the radius of the Earth, B_{eq} is the value of the (model) magnetic field at the equator, and $Y(\sin\alpha_0)$ is taken to be the function corresponding to a dipole. (See the
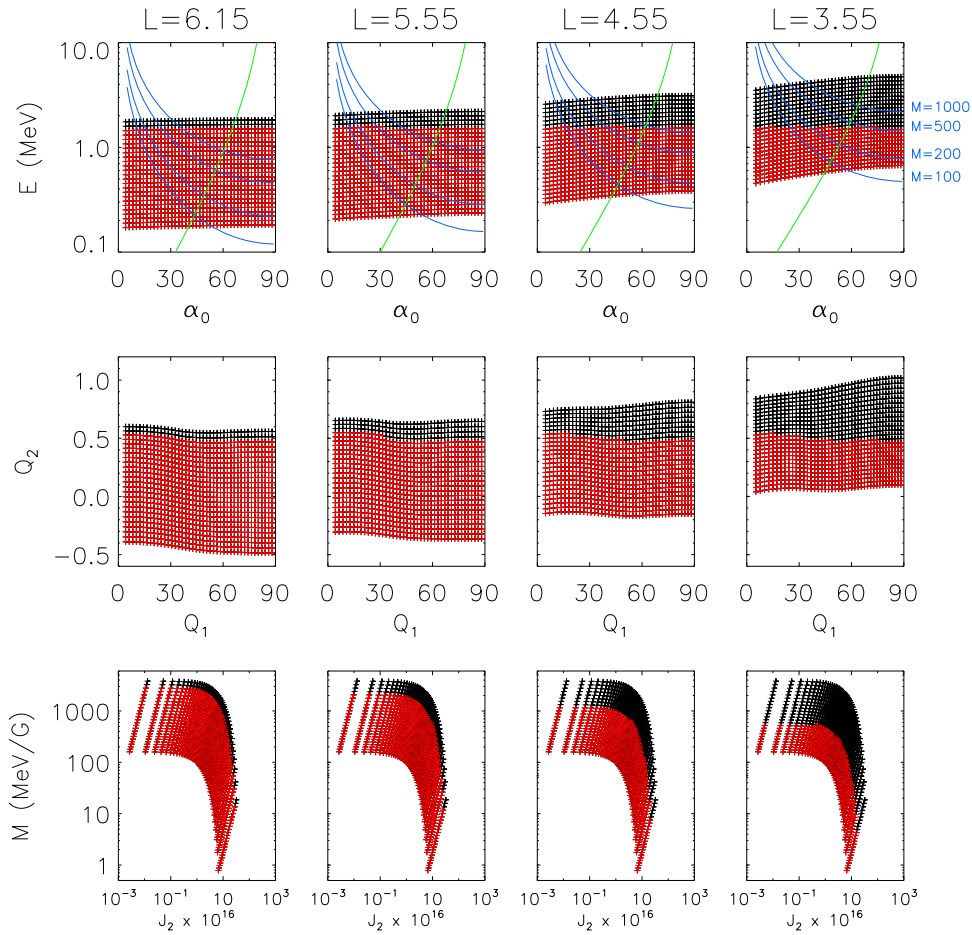
Figure 5. Computational grid points in 2-D for $Kp < 2$, expressed in several sets of variables. The red points are in the range of the CRRES MEA detector. The blue curves indicate several values of first adiabatic invariant M, in MeV/G. The green curves indicate the reference value $J_2 = 1.78 \times 10^{-16}$ g(cm/s)R_e.

discussion in section 2.) The sets of α_0 values were averaged to assign a single α_0 to each L_k, local pitch angle bin, and time interval (t_1, t_2). Schematically, these steps are

$$(\mathbf{x}, B)(t) \rightarrow \{K, L\}(t) \rightarrow \{\alpha_0, L\}(t) \rightarrow (\{\alpha_0\}, L_k)(t_1, t_2), \quad (7)$$

where the braces indicate a set corresponding to the 18 different values of local pitch angle α.

[20] Flux measurements taken during each interval (t_1, t_2) were identified, and log(j) was time averaged for each value of α and E to uniquely specify j as a function of α_0, E, and $\bar{t} = (t_1 + t_2)/2$. Next, since the data were far too sparse to cover all values of α_0, the flux was fit to a function of the form $A \sin^n \alpha_0$ for each MEA energy channel (or, if n was negative, j was simply averaged, equivalent to setting $n = 0$). Interpolating in α_0, where the data were sufficient, yields the flux values shown in Figure 6. In making this plot of $j(L, t)$, the constant value $J_2 = 1.78 \times 10^{-16}$ g(cm/s)R_e was chosen. This follows *Brautigam and Albert* [2000], who were performing 1-D simulations of $f(L, t)$ at constant values of J_1 and J_2 and determined that this value of J_2 maximized the overlap with the available data. This should remain roughly true, even though a different magnetic field model is used here, and allows for at least rough correspondence to the previous work.

[21] The data coverage was then extended by extrapolating the $A \sin^n \alpha_0$ fits beyond the measured values and by linear interpolation and extrapolation of log j in log E. Finally, for arbitrary times t, linear interpolation of log $j(t)$ was performed at fixed (α_0, E, L). This allows j to be evaluated at any grid point (α_i, E_j, L_k) at any time. Schematically,

$$[\{j\}](t) \rightarrow [\{j\}](t_1, t_2) \rightarrow [A, n](\bar{t}) \rightarrow [j(\alpha_0)](\bar{t}) \rightarrow j(\alpha_i, E, \bar{t})$$
$$\rightarrow j(\alpha_i, E_j, L_k, t), \quad (8)$$

where the brackets refer to a set corresponding to the 17 different energy channels of MEA. The results are shown in Figure 7, for the same fixed value of J_2. (No values are shown below $L = 4.2$ for 0.42 MeV, because this is off the computational grid.) These fits, interpolations, and extrapolations of the available data are regrettable but unavoidable if values are to be determined (or assigned) to the entire computational grid.

[22] Once determined, the fluxes were converted to phase space density and are shown in Figure 8 at fixed values of first adiabatic invariant $M = J_1$ (given in units of MeV/G).
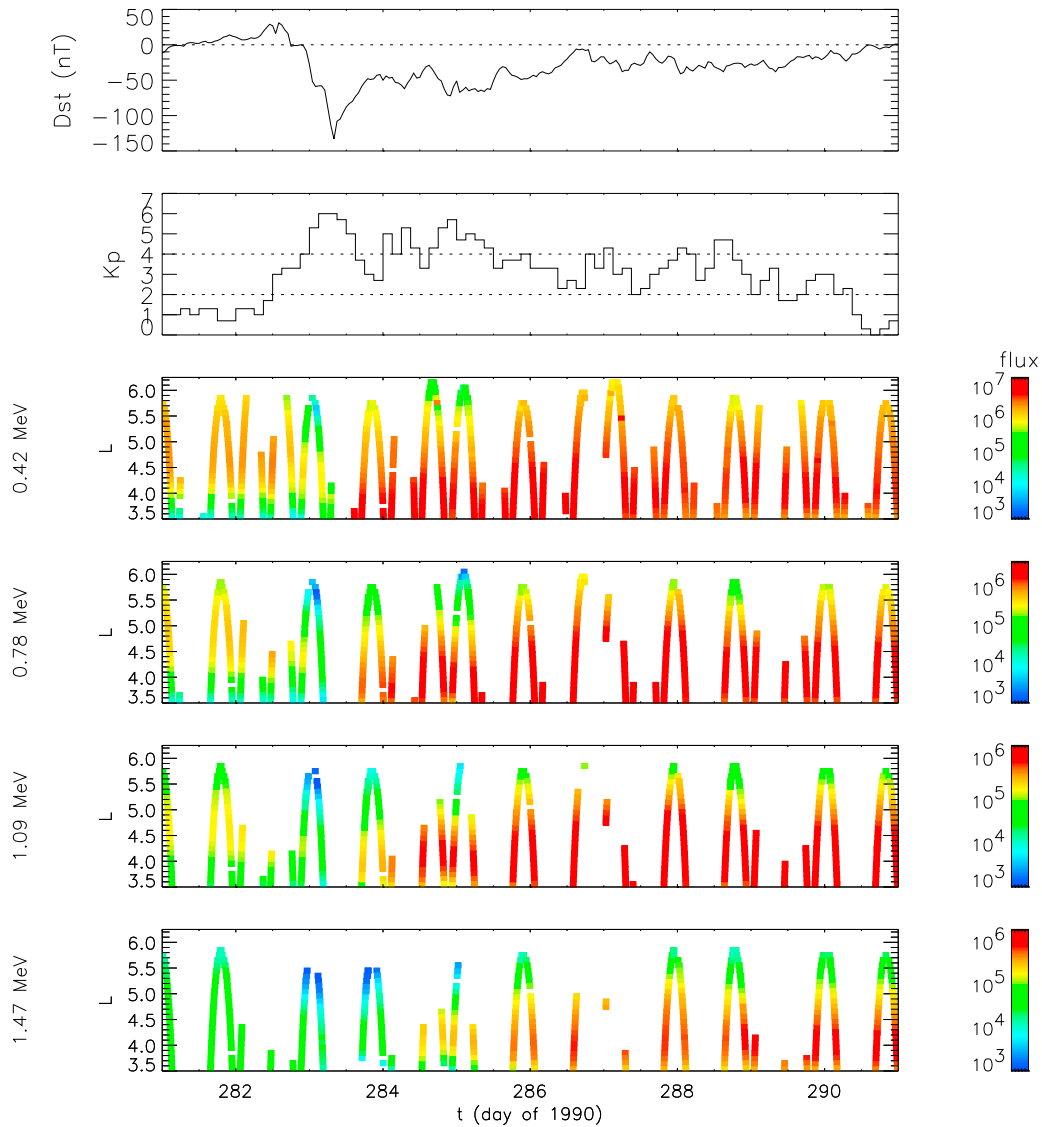
Figure 6. Electron flux as measured by CRRES MEA, in units of number per (cm^2 s sr MeV), as well as *Dst* and *Kp*.

These values are now taken to represent the actual data and will be used to initialize the simulations, to drive them at the boundaries, and for comparison to the results.

4. Simulations

[23] Data from CRRES MEA were processed as just described, for the interval 8–18 October 1990 (day of year 281–291). *Dst* for that interval is shown in Figure 6 and indicates a moderate geomagnetic storm beginning during 9 October (day 282 of 1990). As discussed in detail by *Brautigam and Albert* [2000], a storm sudden commencement at 1315 UT (time 282.54) was accompanied by strong flux decrease at $L = 5$ for $E = 0.42–1.47$ MeV. This was followed by an injection of several hundred keV electrons at $L > 6$ an hour into the recovery phase (time 283.37). Within the next 5 h (by time 283.58), ~100 keV electron flux at $L = 3–6$ had greatly increased, while ~1 MeV flux increased much more gradually. This trend of increase near $L = 5$ was interrupted by notable dips around

$t = 285.0$ and $t = 288.5$. This behavior is reproduced in the interpolated and extrapolated data of Figure 7.

[24] The corresponding values shown in Figure 8 were not only to initialize the simulation but also for time-dependent boundary values on all six planar faces of the 3-D simulation domain. Thus, both radial diffusion and local heating were supplied with realistic, dynamic "seed populations" from which to generate flux at relativistic energies. Grid resolution was 43 values of Q_1, 25 points in Q_2, and 27 points in L, covering $3.55 \leq L \leq 6.15$ with $\Delta L = 0.10$, $\Delta \alpha_0 \approx 2°$, and $E_{j+1}/E_j \approx 1.1$ (although only in L was the spacing constant, as discussed). For simplicity, a fully explicit finite differencing scheme was used, which limited the time step by the Courant-Friedrichs-Lewy condition for linear stability, namely,

$$\max\left[\frac{D_1}{(\Delta Q_1)^2} + \frac{D_2}{(\Delta Q_2)^2} + \frac{D_{LL}}{(\Delta L)^2}\right]\Delta t_{CFL} < \frac{1}{2}. \quad (9)$$
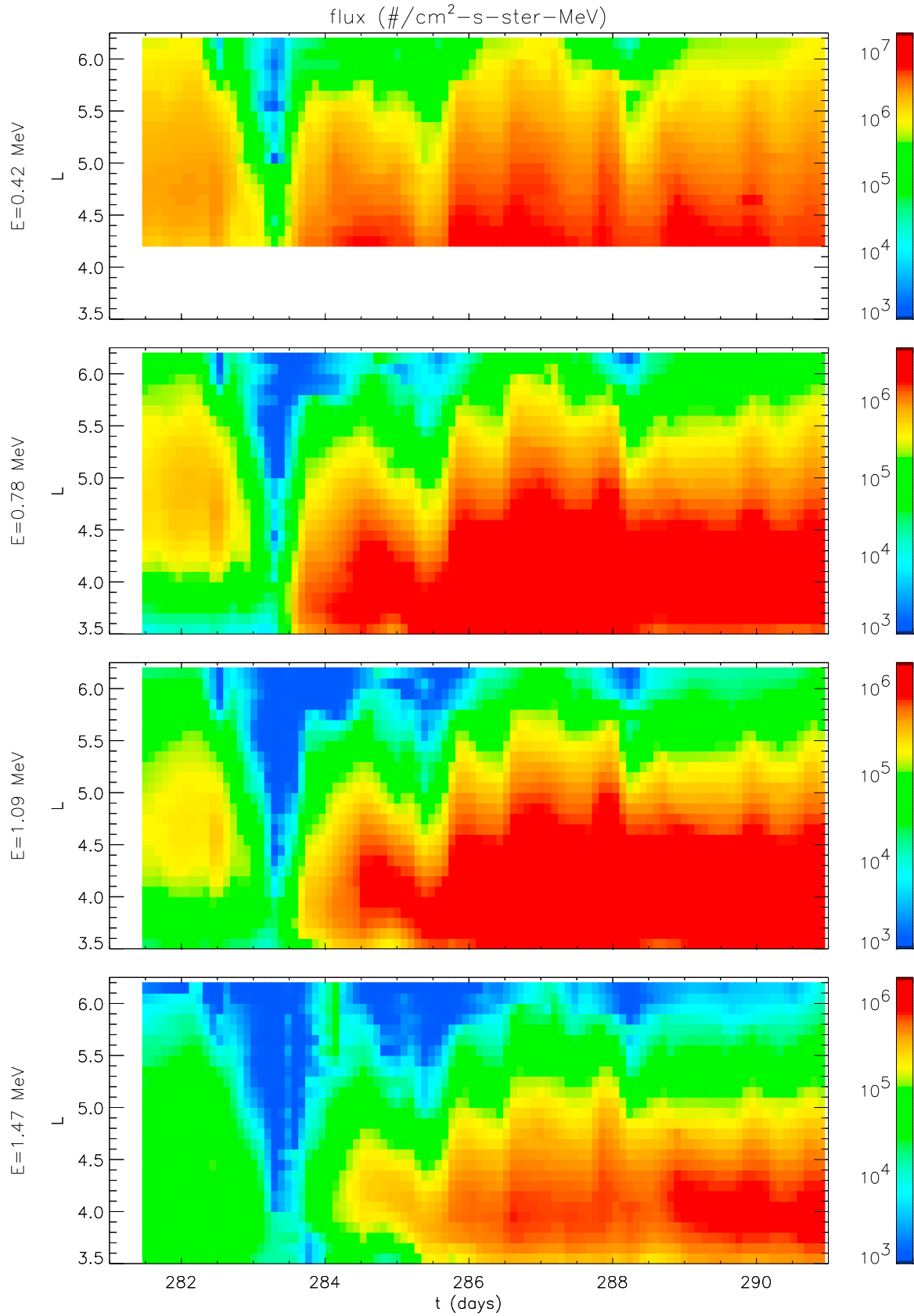
Figure 7. CRRES MEA electron flux, interpolated and extrapolated to cover the computational grid.
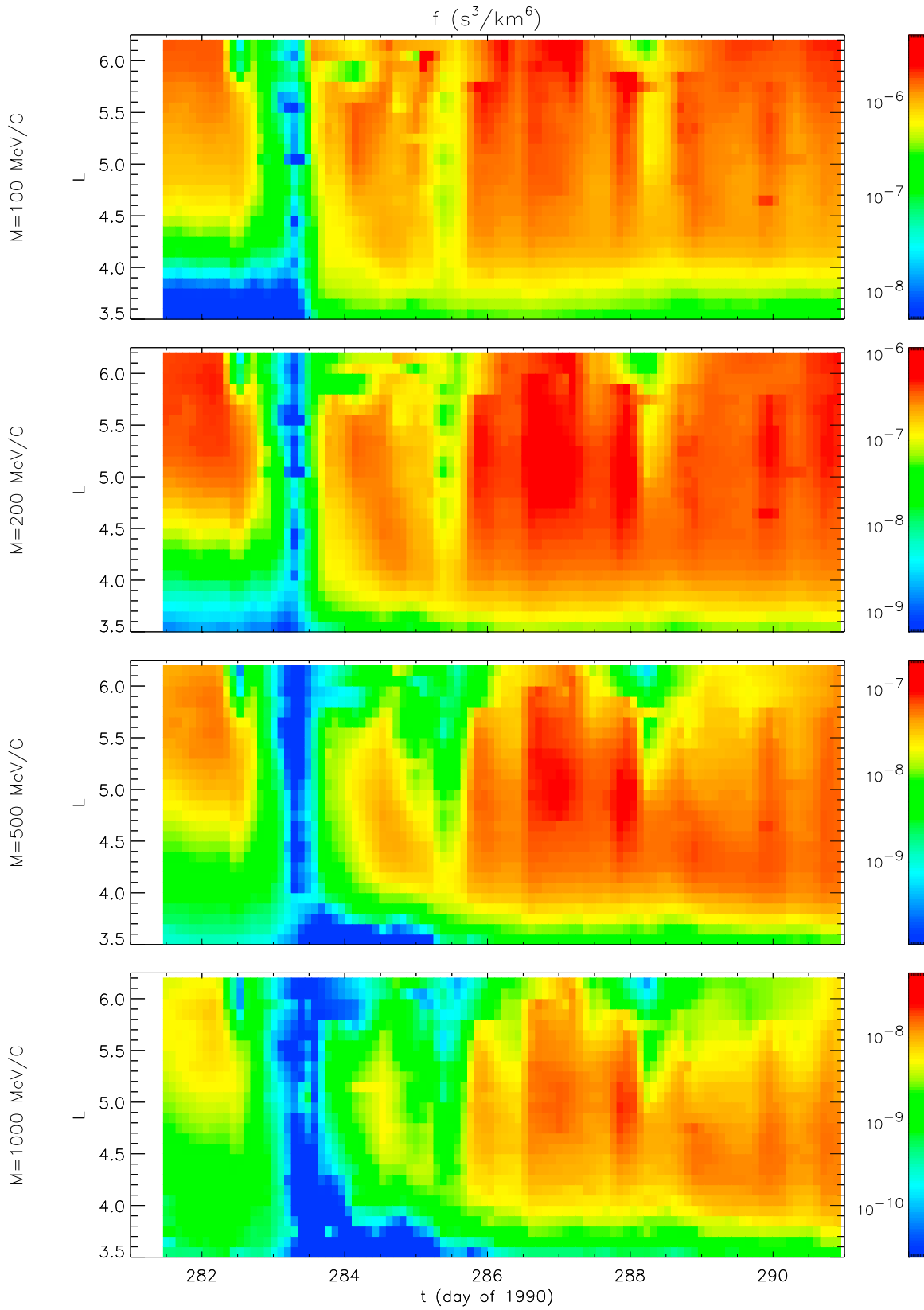
Figure 8. CRRES MEA electron flux, interpolated, extrapolated, and converted to phase space density f.

The actual time step was taken to be $0.5\Delta t_{CFL}$ and was reevaluated whenever Kp changed. This resulted in $\Delta t \approx 16$ s for $Kp < 2$, $\Delta t \approx 4.3$ s for $2 \leq Kp < 4$, and $\Delta t \approx 0.77$ s for $Kp \geq 4$. The entire 9.5 day simulation ran in about 50 min on a standard PC.

4.1. Overview

[25] As mentioned, the value $J_2 = 1.78 \times 10^{-16}$ g(cm/s)R_e was used for the comparisons. First, the wave-induced pitch angle and energy diffusion were omitted, leaving just radial diffusion. Results are shown in Figure 9 and qualitatively reproduce the results of *Brautigam and Albert* [2000]. In particular, fairly good agreement with the measurements (shown in Figure 8) is found for $M = 100$ and $M = 200$ MeV/G, although the dropouts around $t = 283$ are too weak, while the increases for $M = 500$ and $M = 1000$ MeV/G starting around $t = 286$ are far too weak and transient. As noted by *Brautigam and Albert* [2000], the results are essentially driven by transport of the time-dependent values at the outer radial boundary, $L = 6.15$. As found previously, this is sufficient to account for the observed increases at lower L for $M \leq 200$ but evidently not for $M \geq 500$.

[26] Next, a simulation was done with diffusion in (α_0, E) but omitting radial diffusion. As shown in Figure 10, this leads to large, widespread, sustained increase in phase space density for $M \geq 200$, far larger, in fact, than seen in the data, especially at $L > 4.5$. Finally, allowing diffusion in α_0, E, and L to operate leads to intermediate values, as seen in Figure 11. *Varotsou et al.* [2008] also found this ordering of phase space density values when including chorus and radial diffusion separately and together. Figure 11 also shows that these intermediate values also match the data of Figure 8 fairly well.

4.2. Detailed Evolution

[27] A more detailed comparison is shown in Figure 12, which shows $f(t)$ from the three simulations at $M = 200$ and $M = 1000$ MeV/G, at several fixed values of L. Results for $M = 100$ are similar to those for $M = 200$, and results for $M = 500$ are similar to those for $M = 1000$. (The corresponding values of E and α_0 can be determined from the top row of Figure 5.)

[28] In all cases, the dropout around $t = 283$ is not fully captured, especially at low L (hence high E), presumably because of wave-induced precipitation not represented in the simulations, such as by hiss (in the plasmasphere and in plumes), electromagnetic ion cyclotron waves, or possibly by fast magnetosonic waves [*Li et al.*, 2007; *Horne et al.*, 2007; *Albert*, 2008]. A check verifies that f at $M = 1000$ does decrease rapidly near the dropout for larger values of J_2 (smaller values of α_0) in response to lower values at the corresponding grid boundary, but evidently the pitch angle diffusion rates are too low for the values shown to change much before the boundary conditions recover. Of course, this is subject to limitations in deriving the boundary conditions from fits to the limited data.

[29] On the other hand, the increases are captured rather well by the combination of radial and chorus diffusion, which works better than either mechanism acting alone. The largest discrepancies are for $M = 1000$ at $L = 4.55$ and

especially at $L = 4.05$, where the small values (at the dropout) are far too large, and the large values (late in the simulation) are too small by about a factor of 2 or 3. For $L \geq 4.55$, the chorus and D_{LL} results usually lie below the chorus-only values and above the D_{LL}-only values. This was evident in the 2-D plots. Thus, chorus seems to act as the source of phase space density, while radial diffusion acts mostly to transport it away. However, at $L = 4.05$ the values from combined chorus and radial diffusion are higher than from either alone, which implies net radial diffusion into, not away from, $L = 4.05$.

[30] It is reasonable to question the development of agreement at late time ($t \approx 290$) from substantial disagreement at earlier times ($t \approx 283$). Therefore, the simulations were repeated starting at $t = 283.4$, when the measured fluxes are near minimum. The results are shown in Figure 13 and are generally seen to revert to the same values as the previous run after a day or two. This indicates that fluxes are determined by transport of the time-dependent sources at the boundaries more than by existing interior values. *Varotsou et al.* [2008] also found that large differences in initial conditions could lead to relatively similar states after about a day. This is not surprising, since the time scales associated with the diffusion coefficients are ~ 1 day, as shown in Figure 3. An exception occurs for $M = 1000$ at $L = 4.05$ for the chorus-only run, which yields f almost as low as the D_{LL}-only run. Here it is very evident that chorus and D_{LL} do not compete, but instead cooperate, to produce the recovery of phase space density.

4.3. Sensitivity to Diffusion Coefficients

[31] As a sensitivity test, the radial and chorus diffusion coefficients were both included but were doubled and halved, separately and together. Starting the simulation at $t = 281.5$, the effects were small for $M = 200$ MeV/G (especially at large L) and substantial for $M = 1000$ MeV/G, as seen in Figure 14. Relative to the "standard" run, shown again as the black curves, increasing D_{LL} (solid blue curve) led to a more realistic, though lagged, dropout around $t = 283.4$ and lower recovered values of f at late times. Decreasing D_{chorus} (dashed red curve) had a similar effect, while increasing D_{chorus} (solid red curve) or decreasing D_{LL} (dashed blue curve) tended to have the opposite effect, leading to larger f both at the dropout and later. Doubling or halving the strength of both processes at the same time (solid and dashed green curves, respectively) tended to produce smaller changes, suggesting that chorus and radial diffusion compete in determining f. However, this interpretation is not consistent with the runs starting at $t = 283.4$, shown in Figure 15, especially for low L and large M. Decreasing the strength of either process, or both, led to considerably lower f, again indicating that here chorus and radial diffusion reinforce each other in producing the recovery of f. Also note that in both Figures 14 and 15, the runs with doubled D_{chorus} produced excellent agreement with the measured values, except for the shallowness of the dropout obtained in Figure 14.

4.4. Radial Profiles

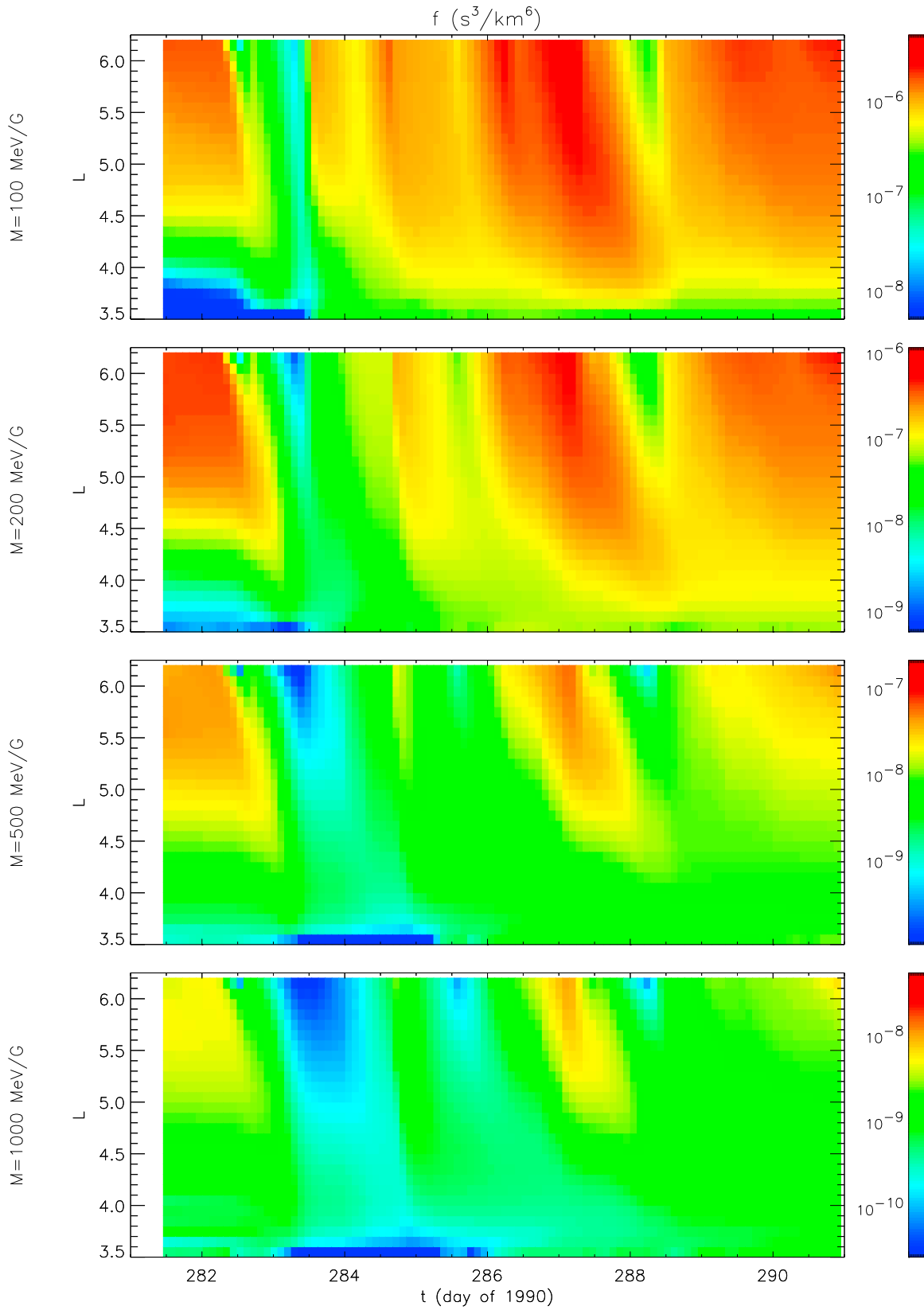[32] Figures 16 and 17 show the simulation results as radial profiles, $f(L)$ at fixed M and J_2. Figure 16 shows

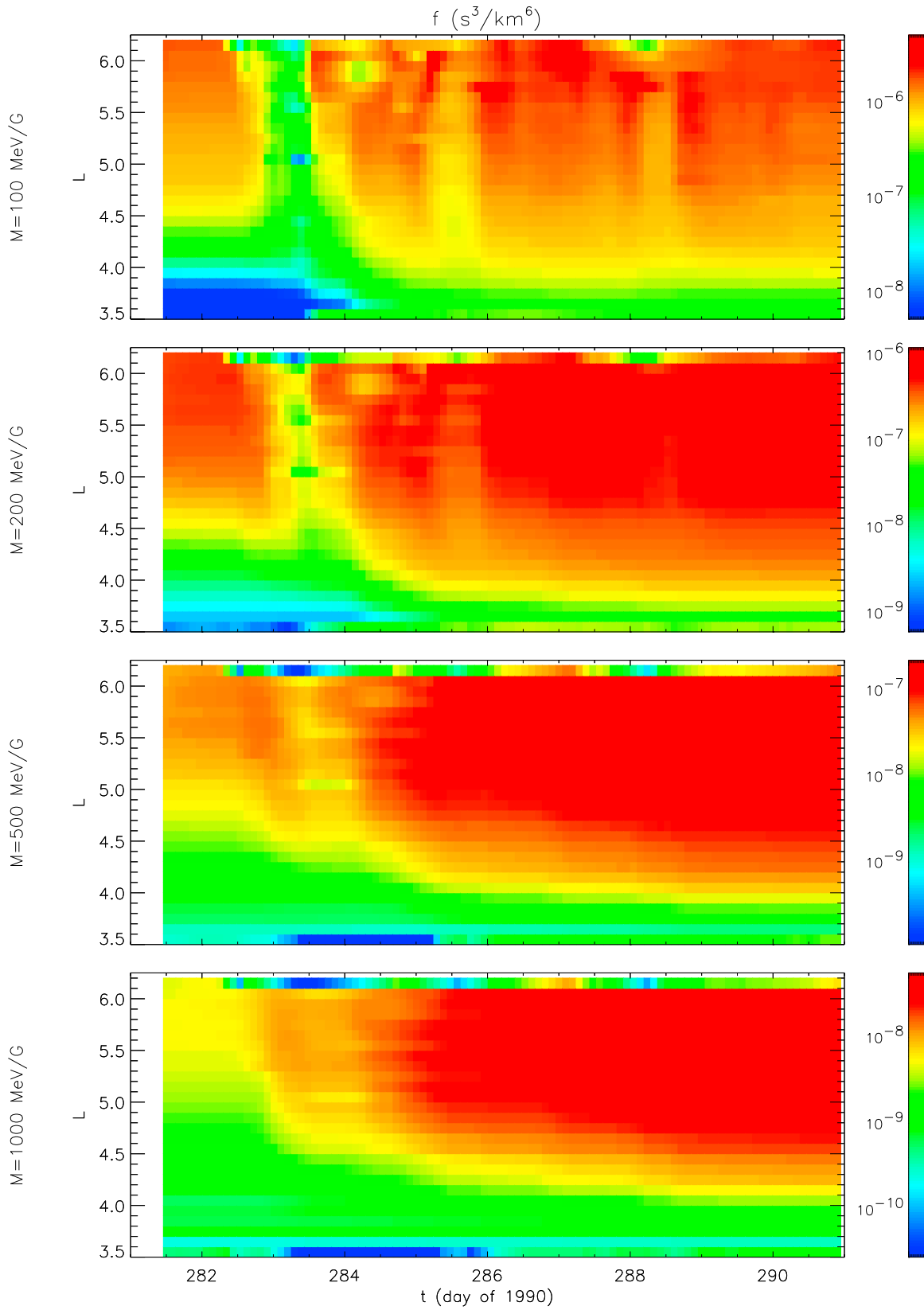**Figure 9.** Phase space density, simulated with radial diffusion only.

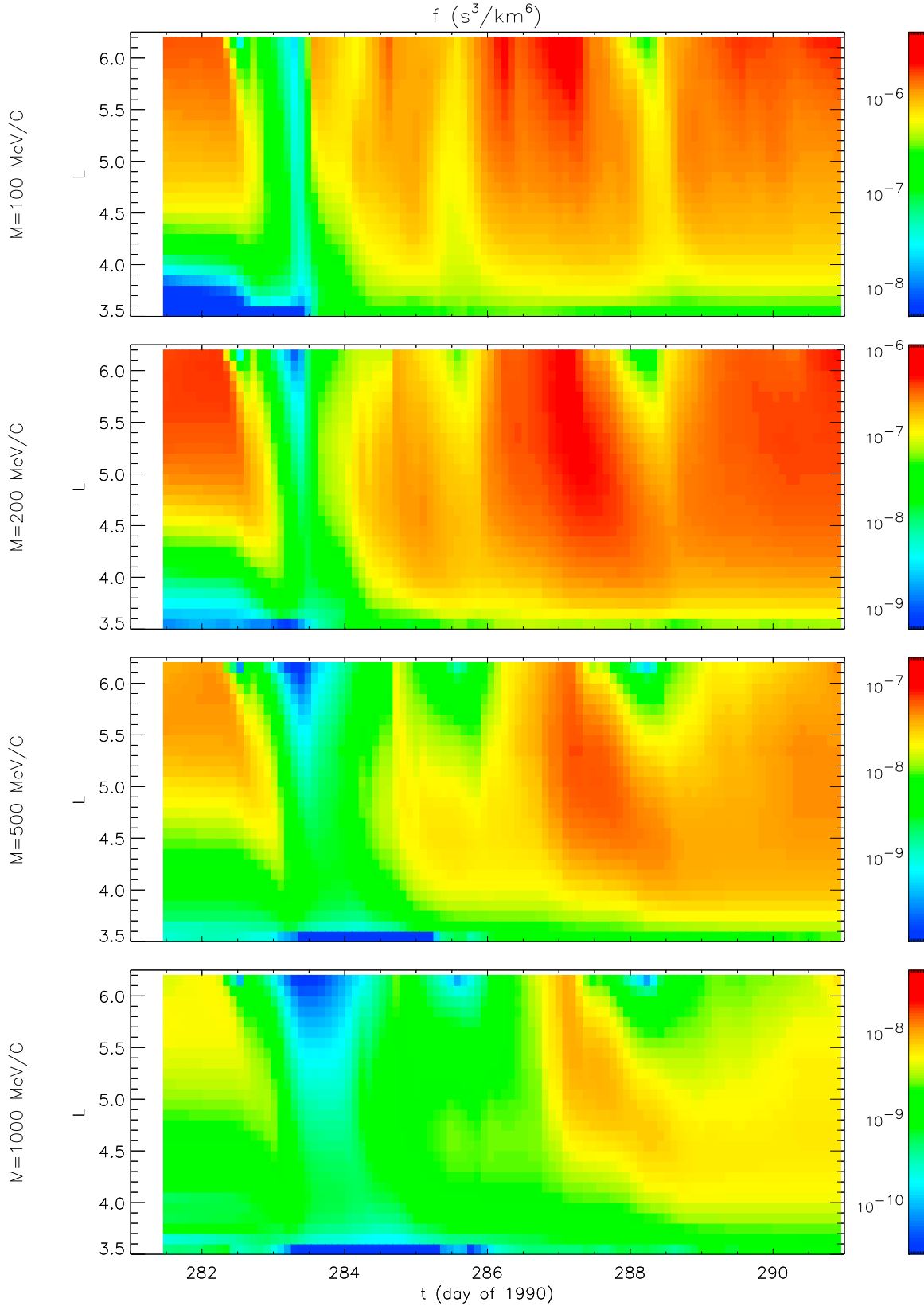**Figure 10.** Phase space density, simulated with chorus diffusion only.

Figure 11. Phase space density, simulated with both radial diffusion and chorus diffusion.
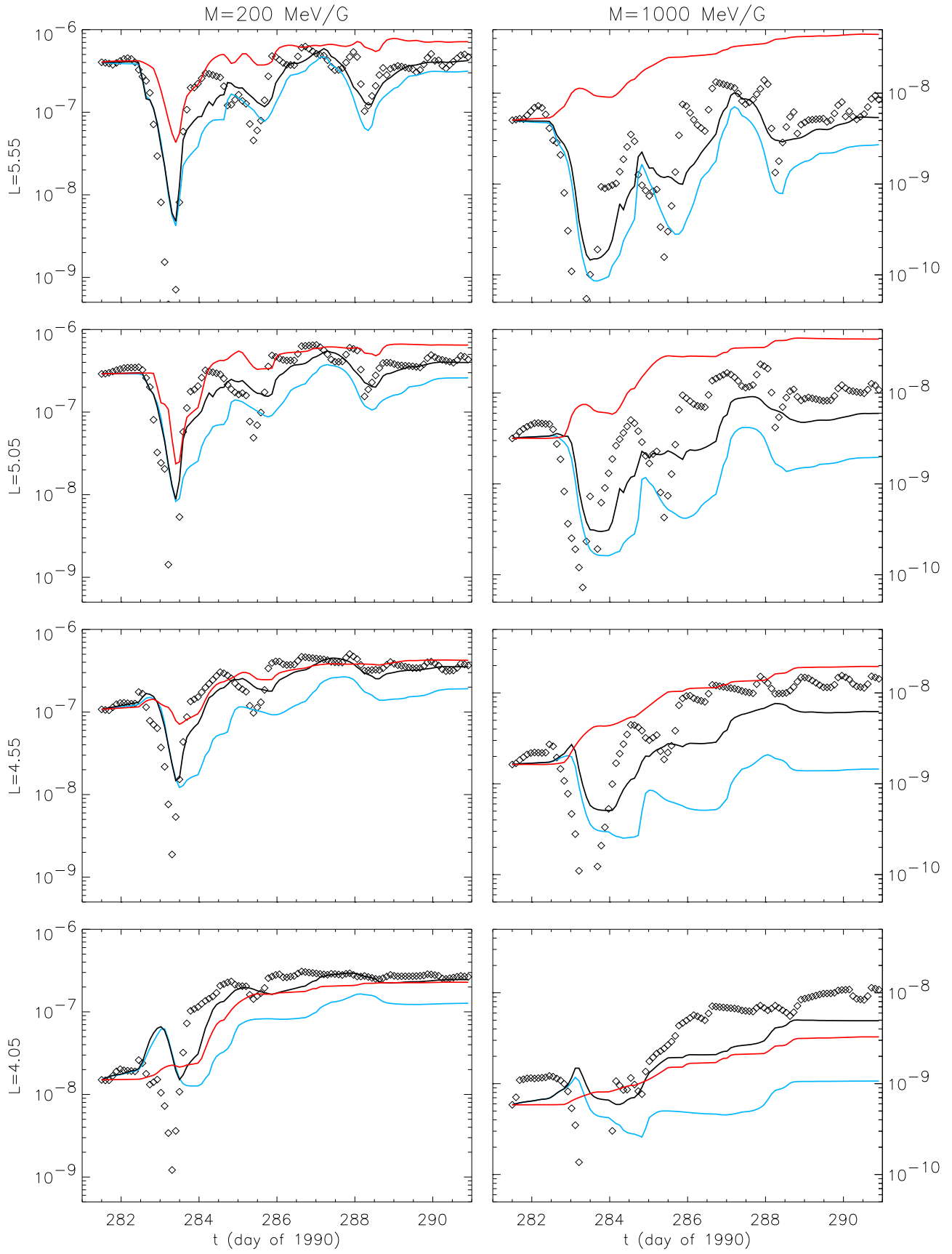
Figure 12. Phase space density, in units of s^3 km^{-6}, as determined from CRRES data (black diamonds), and simulations starting at $t = 281.5$, with D_{LL} only (blue curves), with chorus only (red curves), and with both (black curves).
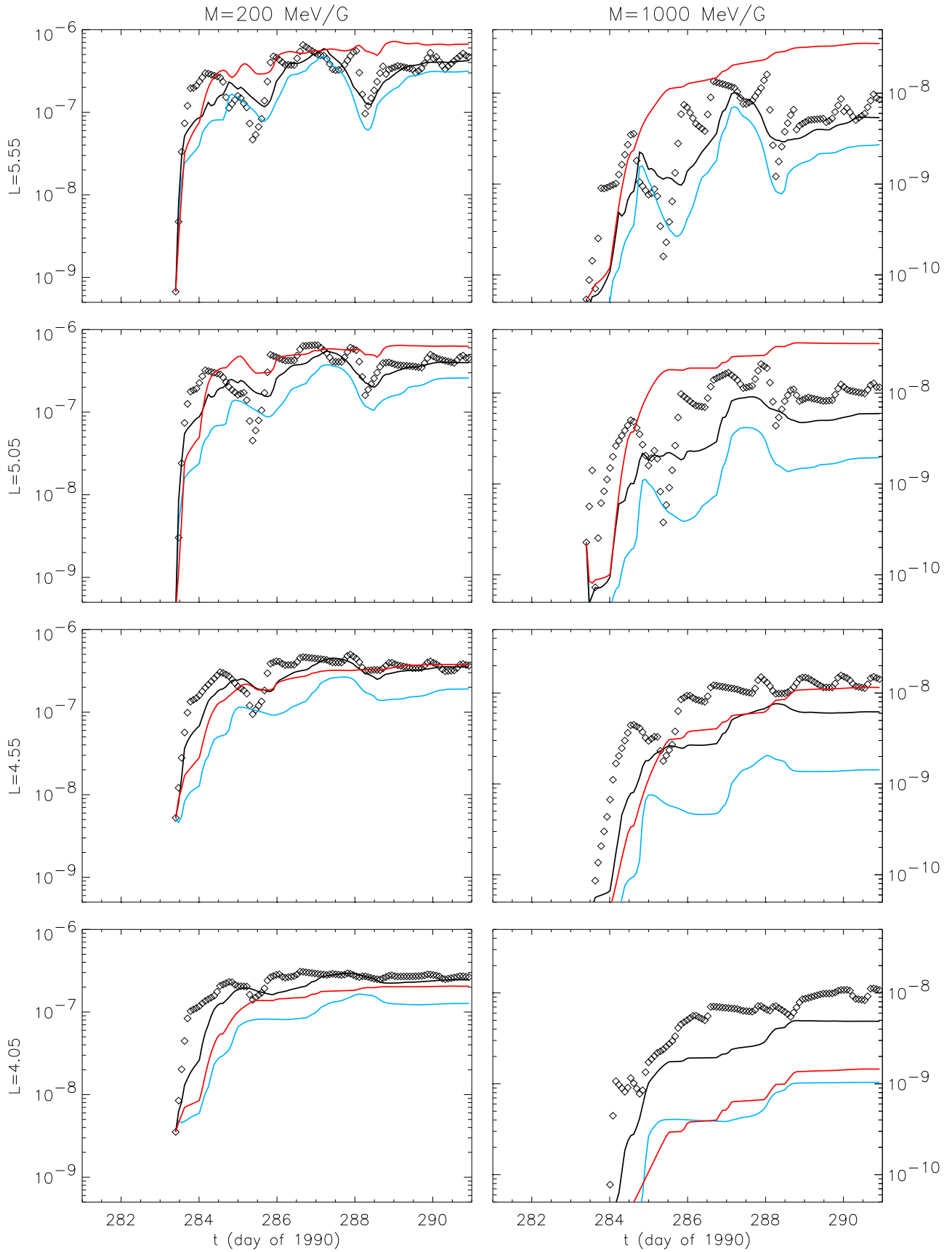
Figure 13. Phase space density, in units of s^3 km^{-6}, as determined from CRRES data (black diamonds), and simulations starting at $t = 283.4$, with D_{LL} only (blue curves), with chorus only (red curves), and with both (black curves).
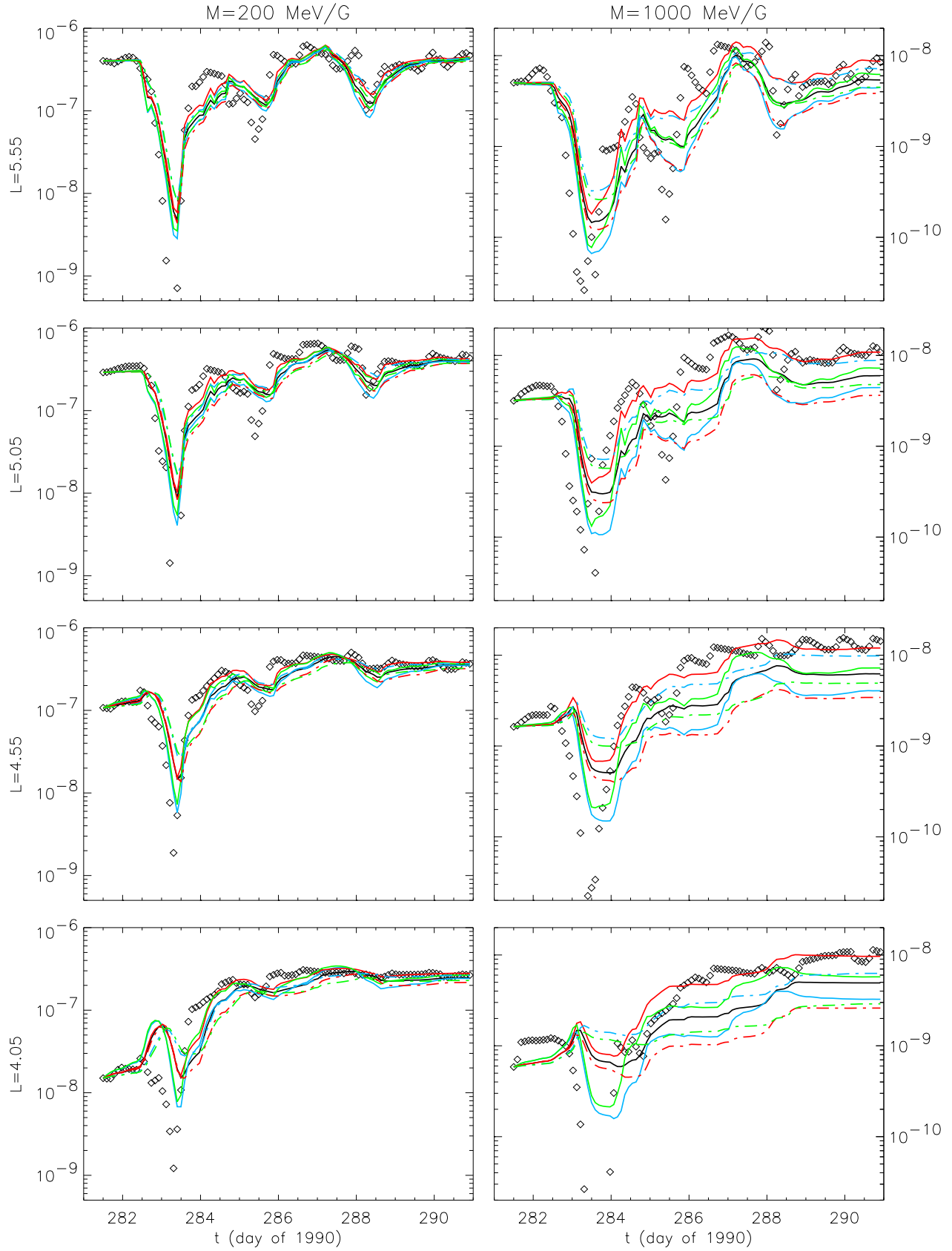
Figure 14. Phase space density as determined from CRRES data (black diamonds) and simulations starting at $t = 281.5$, with both D_{LL} and chorus (black curves), with D_{LL} doubled (solid blue curves) and halved (dash-dotted blue curves), D_{chorus} doubled (solid red curves) and halved (dash-dotted red curves), and with both doubled (solid green curves) and halved (dash-dotted green curves).
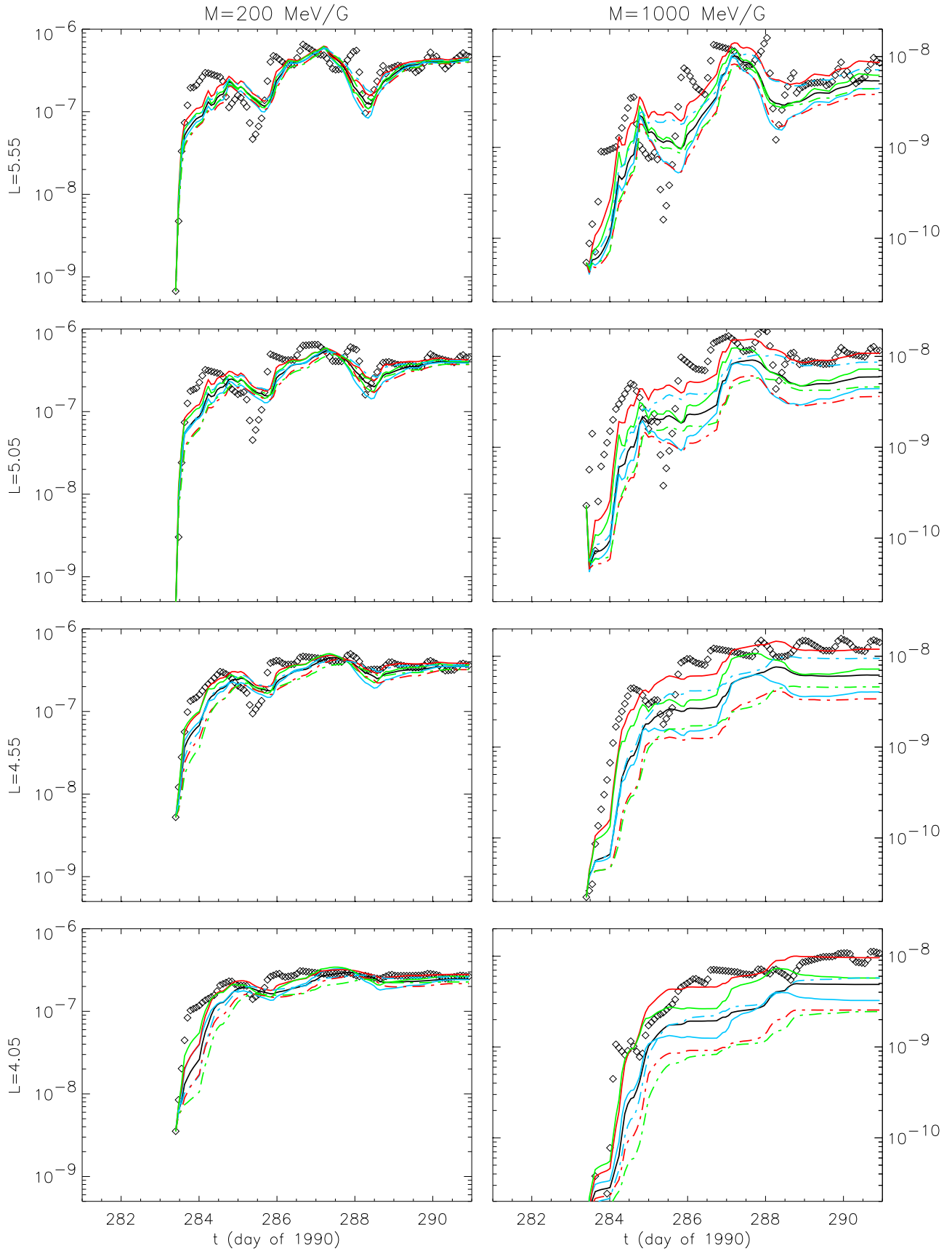
Figure 15. Phase space density as determined from CRRES data (black diamonds) and simulations as in Figure 14, starting at $t = 283.4$.
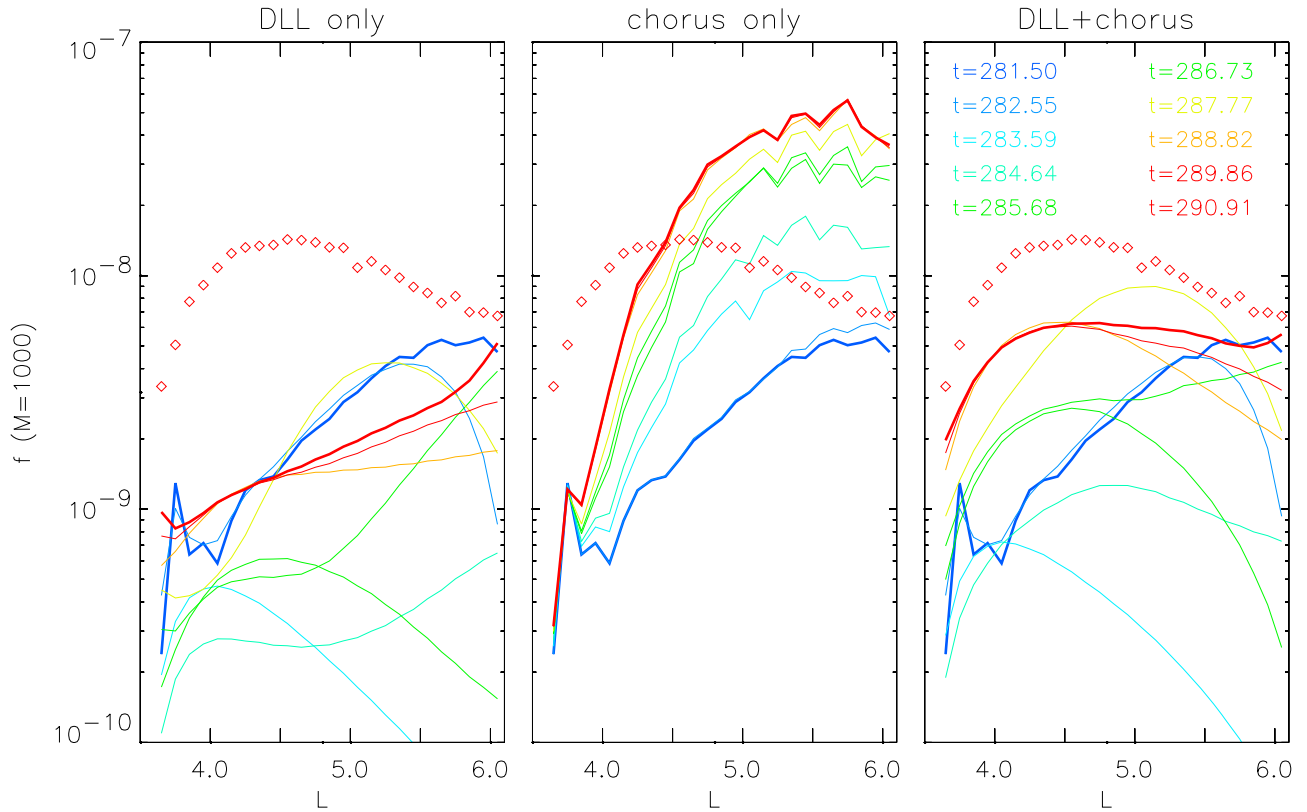
Figure 16. Snapshots of phase space density versus L at various values of t for M = 1000 MeV/G, simulated with D_{LL} only, D_{chorus} only, and both. CRRES data at the end of the simulation is shown as red diamonds in all three plots.

snapshots at several values of t for M = 1000 MeV/G, from the start of the simulations at t = 281.5 to the end near t = 291, as well as the CRRES data at the ending time. The initial profile increases essentially monotonically with increasing L. The simulation with only radial diffusion develops internal peaks, caused by the varying boundary conditions at the maximum and minimum L, but ends up again monotonic and maximum at the outermost L, in qualitative as well as quantitative disagreement with the data. The chorus-only simulation produces profiles that remain monotonic or nearly so, as well as becoming too large. This is contrary to what might be expected from a localized internal source [*Green and Kivelson*, 2004]. The combination of chorus and radial diffusion produces robust internal peaks around L = 4.5 that resemble the data, though they are a bit too low as noted in section 4.2.

[33] Figure 17 shows analogous snapshots of $f(L)$ for several values of M. The curves in Figure 17a, based on the fit CRRES data, start out monotonically increasing with increasing L but quickly develop internal peaks at all M which, for M = 500 and M = 1000 MeV/G, persist throughout the time interval. The simulations with D_{LL}, with or without chorus, reproduce this behavior for M = 100 and M = 200 MeV/G, but without chorus the simulated peaks at M = 500 and M = 1000 are too short lived. The chorus-only run never displays internal peaks. Only the run combining chorus with D_{LL} shows qualitative agreement

with the data throughout the run, at both low and high values of M.

4.5. Effect of Cross Terms

[34] Finally, we briefly consider the effect of omitting the cross-diffusion terms, involving $D_{\alpha_0 P}$. The placement of grid points in (α_0, E) was unchanged, but the coefficient $D_{\alpha_0 P}$ was artificially set to 0, and the numerical procedures (such as tracing constant-Q_2 curves, which become constant-E curves) were carried out as before. Figure 18 shows the ratio of $f(\alpha_0, E)$ with and without cross diffusion at t = 285.5 and L = 4.05 for the chorus-only run starting t = 283.4. As expected from previous 2-D studies with similar chorus models [*Albert and Young*, 2005; *Tao et al.*, 2008, 2009], the effect is concentrated above E = 1 MeV and low values of α_0, with a peak ratio of about 50, and is modest elsewhere. Figure 19 shows how this ratio, evaluated at E = 1.8 MeV and α_0 = 25°, behaves with time (dash-dotted red curve). It is initially 1 (since the initial conditions are identical regardless of cross terms), but quickly grows to a persistent level of about 10. This case, which simulates the production of electrons of energy ∼1 MeV from a depleted state, is representative of how 2-D simulations of storm time chorus heating are usually performed. However, for the chorus-only run starting at t = 281.5 (red solid curve), the ratio only grows to about 3. More significantly, the runs with both chorus and radial diffusion also show a ratio of about 3, starting from either t = 283.4 (dashed black curve) or t = 281.5 (solid black curve). Thus, at least for the diffusion
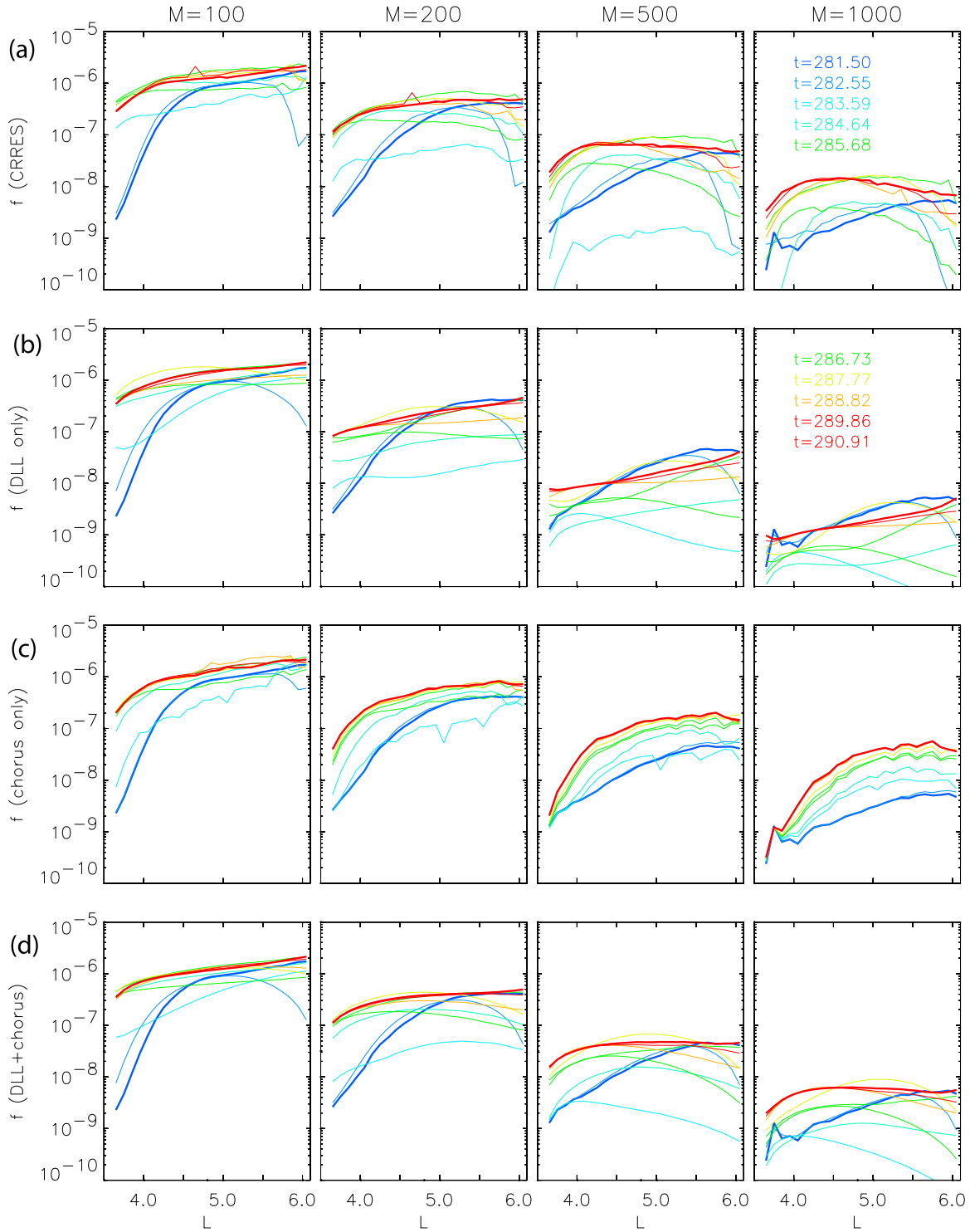
Figure 17. Snapshots of phase space density versus L at various values of t, determined from (a) CRRES data, and (b) simulated with D_{LL} only, (c) D_{chorus} only, and (d) both.

models used here, the substantial effect of the cross terms in 2-D simulations is considerably reduced in the presence of radial diffusion.

5. Summary and Discussion

[35] In summary, we have performed a 3-D simulation of the 9 October 1990 magnetic storm accounting for radial

diffusion and chorus wave-induced diffusion in pitch angle and energy, including cross terms. Grid points were aligned in a natural way for L diffusion (at constant M and J_2), while at each L a grid in (Q_1, Q_2) was constructed for the chorus diffusion. In the spirit of *Brautigam and Albert* [2000], CRRES MEA particle data have been used to obtain realistic, time-dependent boundary conditions, which are transported throughout the computational domain using
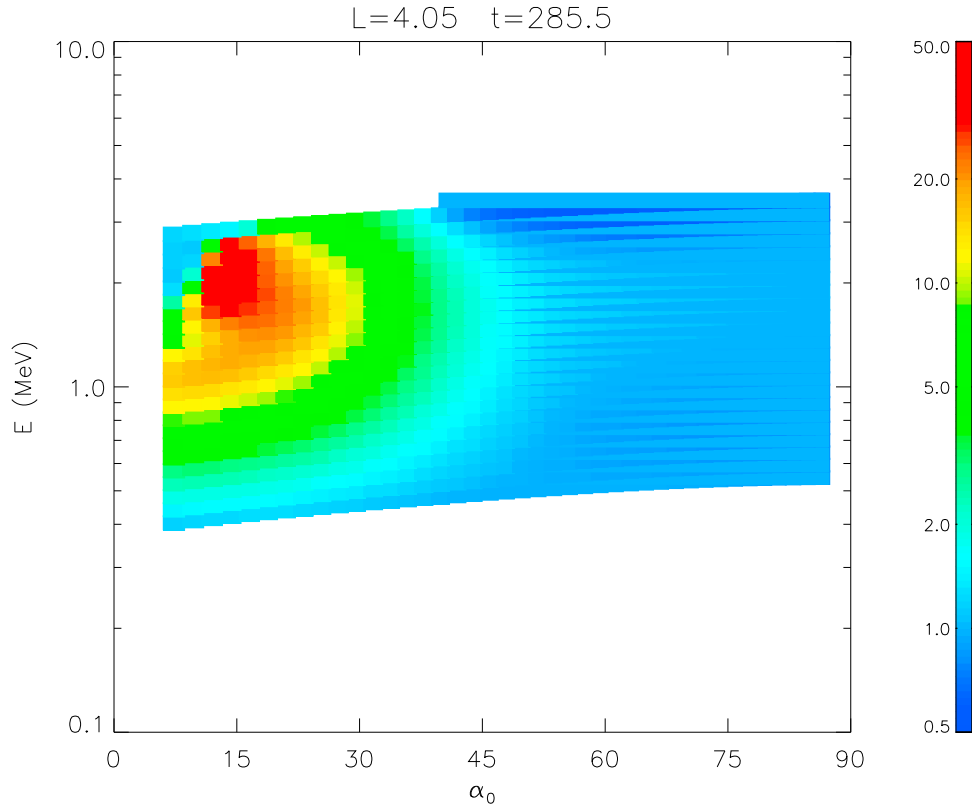
Figure 18. Ratio of simulated f without cross diffusion to f with cross diffusion, at $L = 4.05$, $t = 285.5$, for the chorus-only run starting at $t = 283.4$.

activity-dependent diffusion coefficients. The resulting agreement with data is reasonably good, especially when chorus diffusion is increased by a factor of 2, except for the depth of the main phase dropout. However, this effect of this deficiency is short lived, since runs initialized before and immediately after the dropout quickly converge to each other. (The beneficial factor of 2 for D_{chorus} should not be taken too literally, given the uncertainties in the wave models.)

[36] Experimentation shows that the 3-D combination of D_{LL} and chorus is essential and that either process alone does not give even rough quantitative agreement with the
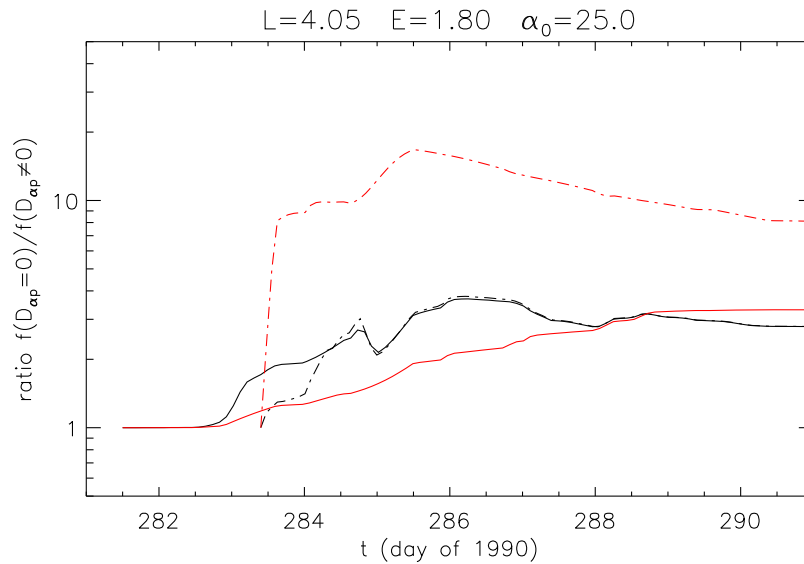

Figure 19. Ratio of simulated f without cross diffusion to f with cross diffusion, at $L = 4.05$, with chorus only (red) curves and with both D_{LL} and chorus (black curves), starting at $t = 281.5$ (solid curves) and at $t = 283.4$ (dash-dotted curves).

persistent internal peaks seen in the data. Such phase space density peaks are a common feature seen during magnetic storms [e.g., *Green and Kivelson*, 2004; *Iles et al.*, 2006; *Chen et al.*, 2007]. Furthermore, the combination of the two processes is complex, since chorus can cause either increase phase space density through energy diffusion or decrease it by pitch angle diffusion, and radial diffusion can act to either increase or decrease f depending on gradients. Thus, simple interpretations based on "competition," or indeed "cooperation," can be misleading. The three-dimensional simulations presented here support the paradigm of inward radial diffusion of lower-energy "seed" electrons which are energized by chorus waves, and then radially diffused both inward and outward, resulting in the observed internal peaks [*Horne*, 2007].

[37] As indicated, the reasonable success in reproducing the CRRES data for this storm depended on having boundary values on all six of the grid boundaries, which raises the question of practicality for space weather forecasting. While it is not unreasonable to presume the availability of data at all needed values of (α_0, E) at L_{min} and L_{max}, one cannot count on having a time series measurements at, say, all (α_0, L) at fixed E_{min}. However, these may be supplied by a ring current code, which almost by definition aims to simulate particles up to lower radiation belt energies.

[38] These results support the effectiveness of simulating chorus-electron interactions by quasi-linear diffusion, despite the increasingly appreciated nonlinear nature of chorus waves. More work is therefore needed not only to develop quasi-linear modeling but to understand why it seems to work as well as it does.

References

Albert, J. M. (2000), Gyroresonant interactions of radiation belt particles with a monochromatic electromagnetic wave, *J. Geophys. Res.*, *105*, 21,191, doi:10.1029/2000JA000008.

Albert, J. M. (2002), Nonlinear interaction of outer zone electrons with VLF waves, *Geophys. Res. Lett.*, *29*(8), 1275, doi:10.1029/2001GL013941.

Albert, J. M. (2004), Using quasi-linear diffusion to model acceleration and loss from wave-particle interactions, *Space Weather*, *2*, S09S03, doi:10.1029/2004SW000069.

Albert, J. M. (2005), Evaluation of quasi-linear diffusion coefficients for whistler mode waves in a plasma with arbitrary density ratio, *J. Geophys. Res.*, *110*, A03218, doi:10.1029/2004JA010844.

Albert, J. M. (2008), Efficient approximations of quasi-linear diffusion coefficients in the radiation belts, *J. Geophys. Res.*, *113*, A06208, doi:10.1029/2007JA012936.

Albert, J. M. (2009), The coupling of pitch angle and energy diffusion, *J. Atmos. Sol. Terr. Phys*, doi:10.1016/j.jastp.2008.11.014, in press.

Albert, J. M., and S. L. Young (2005), Multidimensional quasi-linear diffusion of radiation belt electrons, *Geophys. Res. Lett.*, *32*, L14110, doi:10.1029/2005GL023191.

Bortnik, J., R. M. Thorne, and U. S. Inan (2008), Nonlinear interaction of energetic electrons with large amplitude chorus, *Geophys. Res. Lett.*, *35*, L21102, doi:10.1029/2008GL035500.

Boscher, D., S. Bourdarie, P. O'Brien, and T. Guild (2008), *ONERA-DESP library V4.2*, Toulouse, France.

Brautigam, D. H., and J. M. Albert (2000), Radial diffusion analysis of outer radiation belt electrons during the October 9, 1990, magnetic storm, *J. Geophys. Res.*, *105*, 291, doi:10.1029/1999JA900344.

Chen, Y., G. D. Reeves, and R. H. W. Friedel (2007), The energization of relativistic electrons in the outer Van Allen radiation belt, *Nature Physics*, *3*, 614.

Demekhov, A. G., V. Y. Trakhtengerts, M. J. Rycroft, and D. Nunn (2006), Electron acceleration in the magnetosphere by whistler-mode waves of varying frequency, *Geomagn. Aeron.*, *46*, 711, doi:10.1134/S0016793206060053.

Fei, Y., A. A. Chan, S. R. Elkington, and M. J. Wiltberger (2006), Radial diffusion and MHD particle simulation of relativistic electron transport by ULF waves in the September 1998 storm, *J. Geophys. Res.*, *111*, A12209, doi:10.1029/2005JA011211.

Fok, M.-C., R. B. Horne, N. P. Meredith, and S. A. Glauert (2008), Radiation Belt Environment model: Application to space weather nowcasting, *J. Geophys. Res.*, *113*, A03S08, doi:10.1029/2007JA012558.

Glauert, S. A., and R. B. Horne (2005), Calculation of pitch angle and energy diffusion coefficients with the PADIE code, *J. Geophys. Res.*, *110*, A04206, doi:10.1029/2004JA010851.

Green, J. C., and M. G. Kivelson (2004), Relativistic electrons in the outer radiation belt: Differentiating between acceleration mechanisms, *J. Geophys. Res.*, *109*, A03213, doi:10.1029/2003JA010153.

Horne, R. B. (2007), Plasma astrophysics: Acceleration of killer electrons, *Nature Physics*, *3*, 590.

Horne, R. B., and R. M. Thorne (1998), Potential waves for relativistic electron scattering and stochastic acceleration during magnetic storms, *Geophys. Res. Lett.*, *25*, 3011, doi:10.1029/98GL01002.

Horne, R. B., N. P. Meredith, R. M. Thorne, D. Heynderickx, R. H. A. Iles, and R. R. Anderson (2003), Evolution of energetic electron pitch angle distributions during storm time electron acceleration to megaelectronvolt energies, *J. Geophys. Res.*, *108*(A1), 1016, doi:10.1029/2001JA009165.

Horne, R. B., R. M. Thorne, S. A. Glauert, J. M. Albert, N. P. Meredith, and R. R. Anderson (2005a), Timescale for radiation belt electron acceleration by whistler mode chorus waves, *J. Geophys. Res.*, *110*, A03225, doi:10.1029/2004JA010811.

Horne, R. B., et al. (2005b), Wave acceleration of electrons in the Van Allen radiation belts, *Nature*, *437*, 227, doi:10.1038/nature03939.

Horne, R. B., R. M. Thorne, S. A. Glauert, N. P. Meredith, D. Pokhotelov, and O. Santolik (2007), Electron acceleration in the Van Allen radiation belts by fast magnetosonic waves, *Geophys. Res. Lett.*, *34*, L17107, doi:10.1029/2007GL030267.

Iles, R. H. A., N. P. Meredith, A. N. Fazakerley, and R. B. Horne (2006), Phase space density analysis of the outer radiation belt energetic electron dynamics, *J. Geophys. Res.*, *111*, A03204, doi:10.1029/2005JA011206.

Jordanova, V. J., J. M. Albert, and Y. Miyoshi (2008), Relativistic electron precipitation by EMIC waves from self-consistent global simulations, *J. Geophys. Res.*, *113*, A00A10, doi:10.1029/2008JA013239.

Katoh, Y., and Y. Omura (2007a), Computer simulation of chorus wave generation in the Earth's inner magnetosphere, *Geophys. Res. Lett.*, *34*, L03102, doi:10.1029/2006GL028594.

Katoh, Y., and Y. Omura (2007b), Relativistic particle acceleration in the process of whistler-mode chorus wave generation, *Geophys. Res. Lett.*, *34*, L13102, doi:10.1029/2007GL029758.

Lam, M. M., R. B. Horne, N. P. Meredith, and S. A. Glauert (2007), Modeling the effects of radial diffusion and plasmaspheric hiss on outer radiation belt electrons, *Geophys. Res. Lett.*, *34*, L20112, doi:10.1029/2007GL031598.

Lemaire, J., D. Heynderickx, M. Kruglanski, A. D. Johnstone, D. J. Rodgers, S. Szita, G. Jones, E. Keppler, R. Friedel, and G. Loidl (1998), TREND-3 Radiation Environments of Astronomy Missions and LEO Missions, final report, Eur. Space Res. and Technol. Cent., Noordwijk, Netherlands.

Li, W., Y. Y. Shprits, and R. M. Thorne (2007), Dynamic evolution of energetic outer zone electrons due to wave-particle interactions during storms, *J. Geophys. Res.*, *112*, A10220, doi:10.1029/2007JA012368.

Lyons, L. R., R. M. Thorne, and C. F. Kennel (1972), Pitch-angle diffusion of radiation belt electrons within the plasmasphere, *J. Geophys. Res.*, *77*, 3455, doi:10.1029/JA077i019p03455.

Meredith, N. P., R. B. Horne, R. H. A. Iles, R. M. Thorne, D. Heynderickx, and R. R. Anderson (2002), Outer zone relativistic electron acceleration associated with substorm-enhanced whistler mode chorus, *J. Geophys. Res.*, *107*(A7), 1144, doi:10.1029/2001JA900146.

Meredith, N. P., M. Cain, R. B. Horne, R. M. Thorne, D. Summers, and R. R. Anderson (2003a), Evidence for chorus-driven electron acceleration to relativistic energies from a survey of geomagnetically-disturbed periods, *J. Geophys. Res.*, *108*(A6), 1248, doi:10.1029/2002JA009764.

Meredith, N. P., R. B. Horne, R. M. Thorne, and R. R. Anderson (2003b), Favored regions for chorus-driven electron acceleration to relativistic energies in the Earth's outer radiation belt, *Geophys. Res. Lett.*, *30*(16), 1871, doi:10.1029/2003GL017698.

Nunn, D. (1974), A self-consistent theory of triggered VLF emissions, *Planet. Space Sci.*, *22*(22), 349.

Nunn, D., Y. Omura, H. Matsumoto, I. Nagano, and S. Yagitani (1997), The numerical simulation of VLF chorus and discrete emissions observed on the Geotail satellite using a Vlasov code, *J. Geophys. Res.*, *102*, 27,083, doi:10.1029/97JA02518.

Omura, Y., and D. Summers (2006), Dynamics of high-energy electrons interacting with whistler mode chorus in the magnetosphere, *J. Geophys. Res.*, *111*, A09222, doi:10.1029/2006JA011600.

Roederer, J. G. (1970), *Dynamics of Geomagnetically Trapped Radiation*, Springer, New York.

Schulz, M. (1991), The magnetosphere, in *Geomagnetism*, vol. 4, edited by J. A. Jacobs, pp. 87–293, Academic, San Diego, Calif.

Shprits, Y. Y., and R. M. Thorne (2004), Time dependent radial diffusion modeling of relativistic electrons with realistic loss rates, *Geophys. Res. Lett.*, *31*, L08805, doi:10.1029/2004GL019591.

Shprits, Y. Y., R. M. Thorne, G. D. Reeves, and R. Friedel (2005), Radial diffusion modeling with empirical lifetimes: Comparison with CRRES observations, *Ann. Geophys.*, *23*, 1467.

Shprits, Y. Y., R. M. Thorne, R. B. Horne, S. A. Glauert, M. Cartwright, C. T. Russell, D. N. Baker, and S. G. Kanekal (2006a), Acceleration mechanism responsible for the formation of the new radiation belt during the 2004 Halloween solar storm, *Geophys. Res. Lett.*, *33*, L05104, doi:10.1029/2005GL024256.

Shprits, Y. Y., R. M. Thorne, R. Friedel, G. D. Reeves, J. Fennell, D. N. Baker, and S. G. Kanekal (2006b), Radial diffusion driven by losses at magnetopause, *J. Geophys. Res.*, *111*, A11214, doi:10.1029/2006JA011657.

Shprits, Y., D. Kondrashov, Y. Chen, R. Thorne, M. Ghil, R. Friedel, and G. Reeves (2007), Reanalysis of relativistic radiation belt electron fluxes using CRRES satellite data, a radial diffusion model, and a Kalman filter, *J. Geophys. Res.*, *112*, A12216, doi:10.1029/2007JA012579.

Smith, A. J., N. P. Meredith, and T. P. O'Brien (2004), Differences in ground-chorus for geomagnetic storms with and without enhanced relativistic electron fluxes, *J. Geophys. Res.*, *109*, A11204, doi:10.1029/2004JA010491.

Subbotin, D., Y. Shprits, M. Gkioulidou, S. Merkin, F. Toffoletto, R. Thorne, C. Wang, and L. Lyons (2008), RCM-VERB Coupled simulations of the dynamics of radiation belts during storms, *Eos Trans. AGU*, *89*(53), Fall Meet. Suppl., Abstract SM21A-1651.

Summers, D., and C. Ma (2000), A model for generating relativistic electrons in the Earth's magnetosphere based on gyroresonant wave-particle interactions, *J. Geophys. Res.*, *105*, 2625, doi:10.1029/1999JA900444.

Summers, D., R. M. Thorne, and F. Xiao (1998), Relativistic theory of wave-particle resonant diffusion with application to electron acceleration in the magnetosphere, *J. Geophys. Res.*, *103*, 20,487, doi:10.1029/98JA01740.

Summers, D., C. Ma, N. P. Meredith, R. B. Horne, R. M. Thorne, D. Heynderickx, and R. R. Anderson (2002), Model of the energiza-tion of outer-zone electrons by whistler-mode chorus during the October 9, 1990 geomagnetic storm, *Geophys. Res. Lett.*, *29*(24), 2174, doi:10.1029/2002GL016039.

Tao, X., A. A. Chan, J. M. Albert, and J. A. Miller (2008), Stochastic modeling of multidimensional diffusion in the radiation belts, *J. Geophys. Res.*, *113*, A07212, doi:10.1029/2007JA012985.

Tao, X., J. M. Albert, and A. A. Chan (2009), Numerical modeling of multidimensional diffusion in the radiation belts using layer methods, *J. Geophys. Res.*, *114*, A02215, doi:10.1029/2008JA013826.

Thorne, R. M., Y. Y. Shprits, N. P. Meredith, R. B. Horne, W. Li, and L. Lyons (2007), Refilling of the slot region between the inner and outer electron radiation belts during geomagnetic storms, *J. Geophys. Res.*, *112*, A06203, doi:10.1029/2006JA012176.

Trakhtengerts, V. Y., M. J. Rycroft, D. Nunn, and A. G. Demekhov (2003), Cyclotron acceleration of radiation belt electrons by whistlers, *J. Geophys. Res.*, *108*(A3), 1138, doi:10.1029/2002JA009559.

Tu, W., X. Li, Y. Chen, G. D. Reeves, and M. Temerin (2009), Storm-dependent radiation belt electron dynamics, *J. Geophys. Res.*, *114*, A02217, doi:10.1029/2008JA013480.

Vampola, A. L. (1998), Outer zone energetic electron environment update, in *1997 Conference on the High Energy Radiation Background in Space*, pp. 128–136, Inst. of Electr. and Electr. Eng., New York.

Varotsou, A., D. Boscher, S. Bourdarie, R. B. Horne, S. A. Glauert, and N. P. Meredith (2005), Simulation of the outer radiation belt electrons near geosynchronous orbit including both radial diffusion and resonant interaction with Whistler-mode chorus waves, *Geophys. Res. Lett.*, *32*, L19106, doi:10.1029/2005GL023282.

Varotsou, A., D. Boscher, S. Bourdarie, R. B. Horne, N. P. Meredith, S. A. Glauert, and R. H. Friedel (2008), Three-dimensional test simulations of the outer radiation belt electron dynamics including electron-chorus resonant interactions, *J. Geophys. Res.*, *113*, A12212, doi:10.1029/2007JA012862.

Xiao, F., Z. Su, H. Zheng, and S. Wang (2009), Modeling of outer radiation belt electrons by multidimensional diffusion process, *J. Geophys. Res.*, *114*, A03201, doi:10.1029/2008JA013580.

———————————

J. M. Albert, Space Vehicles Directorate, Air Force Research Laboratory, 29 Randolph Road, Hanscom AFB, MA 01731-3010, USA. (jay.albert@hanscom.af.mil)

R. B. Horne and N. P. Meredith, British Antarctic Survey, Natural Environment Research Council, Madingley Road, Cambridge, CB3 0ET, UK. (r.horne@bas.ac.uk; nmer@bas.ac.uk)